LBL-11971
Preprint c.2

Lawrence Berkeley Laboratory
UNIVERSITY OF CALIFORNIA



Submitted to Physical Review C

# STRONG COULOMB EFFECTS ON PIONS PRODUCED IN HEAVY ION COLLISIONS

J.P. Sullivan, J.A. Bistirlich, H.R. Bowman, R. Bossingham, T. Buttke, K.M. Crowe, K.A. Frankel, C.J. Martoff, J. Miller, D.L. Murphy, J.O. Rasmussen, W.A. Zajc, O. Hashimoto, M. Koike, J. Péter, W. Benenson, G.M. Crawley, E. Kashy, and J.A. Nolen, Jr.

June 1981

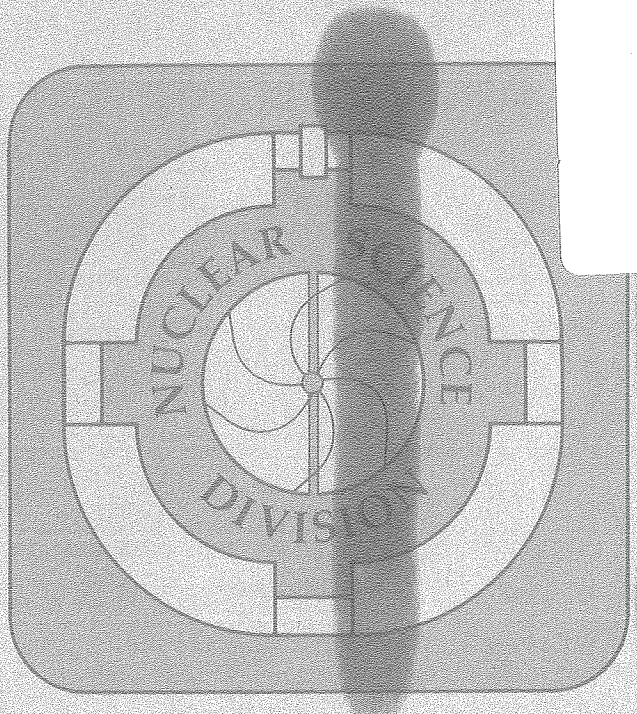




Prepared for the U.S. Department of Energy under Contract W-7405-ENG-48

## DISCLAIMER

LBL-11971

# Strong Coulomb Effects on Pions Produced in Heavy Ion Collisions*

J.P. Sullivan, J.A. Bistirlich, H.R. Bowman, R. Bossingham, T. Buttke, K.M. Crowe, K.A. Frankel, C.J. Martoff, J. Miller**, D.L. Murphy, J.O. Rasmussen, W.A. Zajc
Nuclear Science Division
Lawrence Berkeley Laboratory
University of California
Berkeley, CA 94720

O. Hashimoto, M. Koike
Institute for Nuclear Study
University of Tokyo
Tanashi, Tokyo 188, Japan

J. Péter
Institute de Physique Nucléaire
Orsay, France

W. Benenson, G.M. Crawley, E. Kashy, J.A. Nolen, Jr.
Michigan State University
E. Lansing, Michigan 48824

*This work was supported by the Director, Office of Energy Research, Division of Nuclear Physics of the Office of High Energy and Nuclear Physics of the U.S. Department of Energy under Contract W-7405-ENG-48, by the INS-LBL collaboration program, Institute for Nuclear Study, University of Tokyo, Japan. and by the INS-LBL collaboration program, Institute for Nuclear Study, University of Tokyo, Japan, and by the U.S. National Science Foundation under grant No. 78-22696.

**Present address Boston University, Boston, Massachusetts.

LBL-11971

# Strong Coulomb Effects on Pions Produced in Heavy Ion Collisions

J.P. Sullivan, J.A. Bistirlich, H.R. Bowman, R. Bossingham, T. Buttke, K.M. Crowe, K.A. Frankel, C.J. Martoff, J. Miller*, D.L. Murphy, J.O. Rasmussen, W.A. Zajc
Nuclear Science Division, Lawrence Berkeley Laboratory
University of California, Berkeley, CA 94720

O. Hashimoto, M. Koike
Institute for Nuclear Study
University of Tokyo
Tanashi, Tokyo 188, Japan
and
Nuclear Science Division, Lawrence Berkeley Laboratory
University of California, Berkeley, CA 94720

J. Péter
Institut de Physique Nucléaire
B.P. n°1, 91406 Orsay CEDEX, France

W. Benenson, G.M. Crawley, E. Kashy, J.A. Nolen, Jr.
Michigan State University
E. Lansing, Michigan 48824

## Abstract

Doubly differential cross sections for the production of $\pi^+$ and $\pi^-$ near the velocity of the incident beam for pion lab angles from 0 to 20 degrees are presented. Beams of $^{20}Ne$ with E/A = 280, 380, and 480 MeV and $^{40}Ar$ with E/A = 535 MeV incident on C, NaF, KCl, Cu and U targets were used. A sharp peak in the $\pi^-$ spectrum and a depression in the $\pi^+$ spectrum is observed at 0° near the incident projectile velocity. The effect is explained in terms of Coulomb interactions between pions and fragments of the incident beam. Least squares fits to the data using the Coulomb correction formulas of Gyulassy and Kauffmann and an effective projectile fragment charge are made. The relationship between these data and previously measured projectile fragmentation data is discussed and a simple parameterization of projectile mass, target mass, and beam energy dependence of the differential cross sections is given.

## KEYWORD ABSTRACT

NUCLEAR REACTIONS C, NaF, Cu, U ($^{20}Ne,\pi^{\pm}$)X, E/A = 280-480 MeV; C, KCl ($^{40}Ar,\pi^{\pm}$)X, E/A = 535 MeV; measured $\sigma(E_\pi,\theta_\pi)$, $\theta_\pi$ = 0-20°, $\pi$ velocity near beam velocity; deduced projectile fragment charges, Coulomb effects.

*Present address Boston University, Boston, Massachusetts.

## I. Introduction

The mechanism of pion production with heavy ion beams has been the subject of considerable recent experimental and theoretical effort. Much of this interest arose from the hope of investigating long-range coherent effects in the nucleus or of probing the early stages of the interaction of two high energy heavy ions. Previous measurements of charged pion production generally showed a smooth dependence on pion momentum. However, most of these experiments were restricted to laboratory angles of 30° or greater[1-4] or measured only relatively high energy pions[5]. Streamer chamber measurements[6] of $\pi^-$ cross sections cover forward angles, but beam velocity structure was not noted, perhaps because the number of events measured was too small. More recent measurements[7] near 0° showed a strong peak in the $\pi^-$ energy spectrum near the beam velocity and a corresponding dip in the $\pi^+$ spectrum. This work has helped stimulate theoretical treatments which showed the essential role of Coulomb effects due to the projectile remnants in producing this pion structure.[8-11] A large $\pi^-/\pi^+$ ratio has been observed previously near the target (lab) velocity in emulsion experiments with proton[12,13] and alpha[14] beams and with cosmic rays.[15]

The analysis of these experiments showed that detailed measurements of $\pi^-$ and $\pi^+$ differential production cross sections could probe the dynamics of charge density evolution in heavy ion collisions. In order to make more accurate and higher resolution measurements, the detection system employed in the earlier work was improved by using two 3-plane multiwire proportional counters, one near the focal plane of the spectrometer and one behind it. The pions were stopped in a large-area 11-element scintillation range telescope after passing through the wire chambers.

In the discussion below we describe a series of measurements at beam energies per nucleon between 280 and 535 MeV. The measurements were performed near 0° and for pions near the beam velocity. Beams of $^{40}Ar$ and $^{20}Ne$ were used, and the targets ranged from C to U. The results for every case show a very strong Coulomb effect in the $\pi^-/\pi^+$ ratio. Theoretical calculations are also presented which successfully reproduce the Coulomb effects.

## II. Apparatus and Data Analysis

### A. Apparatus

The data reported in this work were all collected at the Berkeley BEVALAC. Beams of $^{20}Ne$ with E/A from 280 to 480 MeV and $^{40}Ar$ with E/A = 535 MeV were used. The targets used were C, NaF (mass numbers are approximately equal to $^{20}Ne$), KCl (mass numbers are approximately equal to $^{40}Ar$), Cu, and $^{238}U$. The target thicknesses were between 0.4 and 1.1 g/cm$^2$. A schematic diagram of the apparatus used is shown in Fig. 1. The target was located between the coils of the dipole magnet which was used as a pion spectrometer. This target position was chosen to achieve a good 180° focal plane at the position of the first of two multi-wire proportional counters (MWPCs) which were used to measure the trajectories of particles in the magnetic field. The second MWPC was followed by a stack of 11 plastic scintillators which was capable of stopping pions with kinetic energies up to 100 MeV. The first two scintillators were thin (0.64 cm) and were used to measure the rate of energy loss of the particles. The pions of interest were then stopped in one or another of the next eight elements of the scintillator stack (2.5-3.8 cm thick). The last scintillator in the stack was 1.3 cm thick

and was used as a veto counter. For each event, the addresses of all wires which were hit and the pulse heights (ADCs) and timing signals (TDCs) from each element of the scintillator stack were recorded on magnetic tape. The data were read by a PDP 11/45 computer from CAMAC using a micro-computer interface (MBD-11).

B. Data Reduction

A field map of all three components of the magnetic field of the spectrometer magnet was measured in order to calculate pion orbits in the magnet, and thus to find the positions at which these orbits would cross the MWPC planes. A Monte Carlo program was used to generate the starting parameters of the trajectories. A fit was then made which provides the radius of curvature ($\rho$), the angle ($\theta$), and the vertical position of the particle at the target ($Z_0$) as a Chebychev polynomial function of the wire chamber hit positions. The fitting method is described by J.C. Alder et al.[16] Energy loss of pions in air and the MWPCs was included in the orbit calculations, so this small ($\leq$1.5%) correction was included in the algorithm used to calculate $\rho$, $\theta$ and $Z_0$.

For each event on magnetic tape, the addresses of the MWPC wires which fired were used to find the trajectories. If a single trajectory was found, the algorithm described above was used to calculate $\rho$, $\theta$ and $Z_0$ for the particle. Some events (ca. 20%) were rejected because these calculated quantities indicated that the event did not come from the target. Momentum-dependent cuts on the energy loss in the first and second scintillators and on the range of the particle in the scintillator stack were then used to identify pions. Protons and electrons were clearly separated from the pions. The muon contamination was estimated to be less than 3% in all cases.

C. Efficiency and Acceptance of the Spectrometer

The acceptance and efficiency of the spectrometer were calculated with the same Monte Carlo program which was used to generate events for the polynomial fits. Pion events were generated with a uniform distribution in momentum space, and a Gaussian beam spot approximately the size of the actual beam spots was assumed. Pions were allowed to decay into muons while going through the spectrometer (with the appropriate half-life). If a decay did occur, the muon was followed through the spectrometer. When the calculated orbit of a pion or muon passed through both MWPCs and then hit the first scintillator in the range stack, a multiple-scattering, energy loss code was used to follow the particle through the scintillator stack. Pions were allowed to react with carbon nuclei in the scintillators using analytic approximations to the $\pi$-C total cross sections given by A.S. Carrol et al.[17] This total $\pi$-C reaction cross section was divided into 1/3 elastic scattering, 1/3 inelastic scattering, and 1/3 pion absorption (treated as a C($\pi$,p)X reaction). The correction due to reactions of pions with carbon nuclei was generally less than 10%, and, since the correction due to reactions with hydrogen is less, the error introduced by ignoring $\pi$p reactions should be small. For each Monte Carlo event, the MWPC wires that would be expected to fire were found from the calculated hit positions. A probability distribution taken from the real data was used to decide how many adjacent wires would fire in each MWPC plane. Any wire that was not working during the experiment was then removed from this list of wires. This procedure allows the MWPC efficiency to be incorporated into the acceptance calculation. The expected ADC signal in each scintillator was estimated from the calculated energy losses. These simulated data were then analyzed in the same manner as the real data.

Since the Monte Carlo events were generated with a probability proportional to $dp^3$, dividing the number of real data events in each bin corrected for blank target background by the number of Monte Carlo events gives the differential cross section $\frac{d^3\sigma}{dp_\pi^3}$ except for the overall factor which converts the relative yield into the cross section. The cross section so determined thus includes corrections due to $\pi$-$\mu$ decay, wire chamber inefficiency, $\pi$ reactions with C nuclei in the scintillators, multiple-Coulomb scattering in the scintillators, effects due to the finite size of the beam spot and any inefficiencies in the analysis program. The statistical uncertainty associated with the Monte Carlo was never larger than 5% and has been included in the quoted statistical errors.

D. Normalization

The beam intensity was monitored with an Ar-$CO_2$-filled ion chamber. In order to reduce the background associated with the beam hitting the ion chamber, the chamber was placed at the last beam focal point prior to the target, 13 meters upstream. The transmission of the beam from the ion chamber through the final pair of quadrupole focusing magnets to the target position was measured with plastic scintillators at reduced beam intensity and with a second ion chamber. The ion chamber was calibrated as described in the previous experiment[7]. Using the ion chamber, the total number of beam particles could be calculated and the cross-section values normalized. We estimate a 30% uncertainty in the absolute normalization. The factors contributing to this uncertainty are listed in Table I.

Secondary reactions of pions or the beam in the target and effects due to neutrons from capture of stopped negative pions by nuclei in the

scintillator stack were neglected. The correction due to secondary reactions would increase the $\pi^+$ and $\pi^-$ cross sections by less than 3%. The correction due to stopped negative pions would increase the $\pi^-$ cross sections by less than 10%.

In addition to the present data, we obtained a small amount of data for $^{20}$Ne + NaF at E/A = 400 MeV. These 400 MeV data were taken at larger lab angles than the data presented here, and overlap both our Ne + NaF → $\pi^+$ data at E/A = 380 MeV (close to 400 MeV) and the data of Nakai et al.[3] at larger lab angles. Using this set of data to extrapolate the $\pi^+$ data reported here, we found that their cross sections are about 30% higher than our present results, and there is good agreement between the slope of cross section versus momentum. The 30% disagreement is within the limits of error on both their absolute normalization and ours. Our results are also 30% lower than those of Nagamiya et al.[1], but their normalization may not be independent of Nakai et al. since the two sets of data were collected simultaneously with common beam monitors. The normalization of another set of $\pi^+$ data taken with this apparatus[18] agrees with the normalization of Wolf et al.[4] for $^{40}$Ar + $^{40}$Ca at E/A = 1.05 GeV. When we compare our new cross sections with those of our earlier work with the Pb-slit-scintillator spectrometer[7], we find that the absolute value of the present results is about 50% of that obtained previously, which is within the quoted uncertainty.

E. Resolution

In comparing cross sections with sharp structure one must take experimental resolution into account. The beam velocity peaks and valleys of the data have widths larger than the resolution, but effects due to the resolution cannot be ignored. This effect was treated by folding the

calculated resolution function into the theoretically calculated cross sections. Factors contributing to the resolution were the size of the beam spot; the spatial resolution of the MWPCs; energy loss in the target; multiple scattering in the target, in air and in the MWPCs; the size of the data bins; and the uncertainty introduced by the use of the polynomial fit to calculate the momenta of the particles. Multiple scattering in the target made the largest contribution to the angular resolution. The momentum resolution was not dominated by any single effect. Table II summarizes the resolution of the spectrometer for pions near the momentum of the observed peaks in the negative pion spectra for the combinations of beam energies and target reported here.

Due to uncertainties in the absolute magnitude of the magnetic field used during the experiment and the position of the beam spot on the target, there is an additional 1.5% uncertainty in the magnitude of the momentum. The beam ranges were measured with aluminum and/or copper wedges and Polaroid film, and the beam energies were calculated from the ranges.[19] All beam and pion energies given here are the values at the center of the target.

## III. Results

Figures 2-5 show cuts through the peak in the $\pi^-$ spectra (hole in the $\pi^+$ spectra) as a function of lab angle and lab momentum for each of the nearly equal mass projectile-target combinations studied. The vertical error bars are statistical. The horizontal error bars on the graphs of cross section vs angle show the angular resolution (given in Table II) and, on the graphs of cross section vs momentum, show the momentum resolution. The solid curves are least squares fits of functions

based on Gyulassy and Kauffmann's[10] theoretical expressions. These solid curves have had the resolution of the spectrometer folded into them. The dashed curves are the same functions before folding with the resolution and the dotted curves are the fitted pion spectra in the absence of Coulomb effects. Figures 6-17 show the data for all projectile-target combinations studied as plots of Lorentz invariant cross sections vs lab momentum at fixed lab angles from 0 to 20 degrees. As in figures 2-5, the vertical error bars are statistical and the solid curves are least squares with the experimental resolution folded in. Numerical tables of all cross sections will be given in reference 20.

In the case of the $\pi^+$ data at E/A = 380 MeV, we have an overlap with Nakai et al.[3] As mentioned earlier, there is a 30% disagreement in normalization. We therefore apply this normalization factor to their data and combine it with our data to produce the Lorentz-invariant cross section contour plot of Fig. 18. Here the approximate symmetry about the center-of-mass has been used to reflect the data sets of both studies about the center-of-mass.

For all the projectile-target combinations which were studied, a peak in the $\pi^-$ differential cross section (and in the $\pi^-/\pi^+$ ratio) was observed slightly lower than the velocity of the incident beam. The shifts of the peaks from the momentum associated with the beam velocity are within our experimental uncertainties, independent of beam energy over the range reported here. For the neon beam this pion momentum shift is $3.2 \pm 1.6$ MeV/c in the rest frame of the incident beam. For $^{40}Ar$ the corresponding shift is $2.0 \pm 1.7$ MeV/c. The depression in the $\pi^+$ cross section near beam velocity is broader than the corresponding $\pi^-$ peak but has approximately the same downshift as does the $\pi^-$ peak.

Table III gives the half-widths, $\Gamma_i/2$, of the peaks in the $\pi^-$ spectra and the pion momentum shifts for each of the projectile-target combinations in the projectile velocity frame. The widths are defined as the half widths at half maximum, measured above a smooth background. The smooth background was defined by the source function which is described below (see eq. 4). The resolution of the spectrometer has been subtracted in quadrature from these widths. In Table III the widths of the peaks are expressed in terms of parallel and perpendicular momentum; if they had been defined in terms of pion kinetic energies in the beam velocity reference frame, the full widths at half maximum would generally be less than 1 MeV.

## IV. Discussion

### A. Coulomb Correction Equations

The theory of Gyulassy and Kauffmann[10] (GK) has been used to fit the $\pi^\pm$ data. In their work, approximate Coulomb correction formulas are developed, using a perturbative approach to treat both quantum and relativistic effects due to the field of thermally expanding charge distributions. The charged pion cross sections are given in terms of an uncharged pion cross section evaluated at a momentum which has been shifted by a Coulomb impulse, then modified by a Coulomb phase space distortion factor. The "non-perturbative" extrapolation of the GK model has been used in this analysis.

$$\sigma_\pm(\vec{p}) = \sigma_0(\vec{p} \mp \delta\vec{p})G(\pm\delta D/\pi) \qquad (1)$$

where

$\sigma_o(\vec{p})$ = the uncharged pion source function $(d^3\sigma/dp_\pi^3)$

$\vec{p}$ = the observed momentum of the particle

$\delta\vec{p}$ = the Coulomb impulse

$\delta D$ = the Coulomb phase space distortion factor, and

$G(\eta)$ = Gamow factor = $2\pi\eta/[\exp(2\pi\eta) - 1]$.

The uncharged pion source function is evaluated at a shifted momentum, and the momentum shift is given by GK as

$$\delta\vec{p}_\mu(\vec{p}) = \sum_i Z_i\alpha(q - E_i'u_i/c)_\mu \frac{E_i'R_i\hbar c}{(\hbar c)^2 + (p_i'cR_i)^2} \qquad (2)$$

where the parameters associated with the charged fragments are

$Z_i$ = charge on fragment i

$R_i = \left\langle\frac{1}{r}\right\rangle^{-1}$ = mean inverse radius of fragment i.

$T_i$ = temperature of fragment i in MeV

$\beta_{Ti}^2 = \frac{\pi T_i}{2m_pc^2}$ = T/597 MeV = mean square thermal velocity of protons

$u_i$ = 4 - velocity of fragment i = $(\gamma_i, \gamma_i\vec{\beta}_i)$, $\gamma_i = (1-\beta_i^2)^{-1/2}$

and the kinematic variables are

$E_i$ = energy of particle in the rest frame of charge i (mass + kinetic) = $q_\mu u_i^\mu = (E/c)\gamma_i - \vec{p}\cdot\vec{u}_i$

$E_i' = E_i(1 - \beta_{Ti})^{-1/2}$

$q$ = 4-momentum of particle in the frame in which $\delta p_\mu$ is being evaluated = $(E/c, \vec{p})$

$p_i' = [(E_i'/c)^2 - (m_\pi c)^2]^{1/2}$, and

$\alpha = e^2/\hbar c = 1/137$.

We assume

$$R_i = \frac{2}{3} r_o A_i^{1/3}$$

where $A_i$ is the mass number and $r_o$ is taken somewhat arbitrarily as 1.4 fm. The factor of 2/3 relates the mean inverse radius of a uniformly charged sphere to its radius.

The source function is then modified by a phase space distortion factor as shown in equation 1. In that equation

$$\delta D(p) = \pi\alpha \sum_i Z_i \frac{E_i'}{p_i' c} \mathcal{F}(p_i') \qquad (3)$$

$\mathcal{F}$ = script F

where the variables have the same meanings as above, and for the form factor we take

$$\mathcal{F}(p_i') = [(\pi p_i' R/\hbar)^2 + 1]^{-1/2}.$$

Notice that as $p \to 0$, $\delta D/\pi$ reduces to the conventional form for the Sommerfeld parameter ($\eta = Z\alpha/\beta$). Our form factor is not identical to that derived by GK for an exponential charge distribution, but it closely approximates their expression, has the same limits as $p \to 0$ and $p \to \infty$, and is simpler to evaluate.

The sums in equations 2 and 3 are over all charge distributions. We assume that there are projectile and target fragments with charges $Z_p$ and $Z_t$ at relatively low temperatures. Temperatures are parameterized in terms of a thermal velocity ($\beta_{Ti}$) as shown below equation 2. A hot central charge distribution is assumed for all of the charge not contained in the projectile and target fragments.

It was not possible to fit our data or those of ref. 7 with an uncharged source function of a single Boltzmann distribution (the fireball

model[21]) since, in contrast to the predictions of this model, the measured differential cross section ($d^3\sigma/dp^3$) does not always fall with increasing pion energy in the center of mass. We used a source expressed by the lowest three terms in a momentum expansion about the center of mass. A Boltzmann factor exponential with pion "temperature" estimated from Nagamiya et al.[1] was used to give the correct asymptotic behavior.

$$\sigma_o(p,\theta) = N\left[1 + \left(\frac{p_{cm}}{m_\pi c}\right)^2 (c_1 + c_2 P_2[\cos\theta_{CM}])\right]\exp(-E_{cm}/T) \qquad (4)$$

where

$p_{cm}, E_{cm}$ = momentum and total energy (mass + kinetic) of the pion in the nucleon-nucleon center of mass.

$N$ = normalization parameter

$c_1, c_2$ = source shape parameters

$P_2(\cos\theta) = (3\cos^2\theta - 1)/2$

$T$ = slope parameter or temperature of the source

For $c_1 = c_2 = 0$, this expression reduces to a central thermal pion source. Notice that the temperature in equation (4) is not equal to the temperature in equations (2 and 3).

B. Parameters for Least Squares Fits

The normalization (N in equation 4), the source shape parameters ($c_1$ and $c_2$ in equation 4), and the charge on the projectile fragment ($Z_p$) were used as parameters in a least squares fit of this function to our data. The shift of the peak in the $\pi^-$ spectrum (or hole in the $\pi^+$ spectrum) from the velocity of the incident projectile ($dp_{||}$ values in Table III) was estimated graphically and was held fixed during the fitting procedure.

The charge on the target fragment was calculated by assuming that the same number of nucleons were knocked out of the target as were knocked out of the projectile. The charge-to-mass ratio of both the projectile and target fragments were assumed to be the same as in the initial nuclei. The charge and mass of the hot central charge distribution were then calculated by charge and baryon number conservation. The charge of the produced pion was included in the charge balance equation. For the projectile and target fragments, we have fixed the parameter $\beta_{Ti}$ according to measured velocity dispersion of projectile fragments[22-24] (see eq. 6 below). The temperature (in equation 2 and 3) of the central charge distribution was taken to be $T = 2E^*/3$, where $E^*$ is the beam energy per nucleon in the center of mass. Source shape parameters $c_1$ and $c_2$ for $\pi^+$ were taken from corresponding $\pi^-$ fits. In Table IV and Figs. 19-20 we show the values of the parameters found in our fits. The uncertainties associated with the parameters are defined in Appendix I.

C. Results of Fits

The solid curves of Figs. 2-17 show the results of these fits. The resolution of the spectrometer has been folded into these curves. The dashed lines in Figs. 2-5 show the same fitting function before folding with the resolution, and the dotted lines show the uncharged pion source function (see eq. 4). The fits were made as a function of momentum and angle, so the comparisons of the calculations and the data in Figs. 2-5 represent only two cuts through the two-dimensional surface centered on the $\pi^-$ peak and $\pi^+$ hole near beam velocity.

A few words are necessary to explain the physical interpretation we attach to $\beta_{Ti}$, GK's thermal expansion velocity for a cool, but thermally expanding unbound projectile remnant. In addition to the fitting listed

in Table IV we attempted to fit $\beta_{Ti}$ as a free parameter. The $\beta_T$ values for the target fragment so obtained correspond to nucleon temperature values that are unreasonably small, of the order of 1 MeV, which implies that the projectile fragment will be bound and will not expand. These results prompted us to formulate quantitatively the role of bound projectile fragments near beam velocity. In a separate paper Radi et al.[25] have derived expressions for the projectile fragment Coulomb effects. One such expression may be written for pions near the beam velocity as

$$\delta D(\beta_\pi) = \pm\pi Z\alpha/(\beta_\pi^2 + \beta_T^2)^{1/2} \tag{5}$$

In the nonrelativistic limit, equation 3 reduces to equation 5 if the form factor is taken at its limit of unity (corresponding to beam velocity pions) and $\beta_\pi$ is the pion velocity (in units of c) in the projectile spectator reference frame. Our interpretation of the meaning of $\beta_T$ is quite different from that of GK. In our case $\beta_T$ is the r.m.s. velocity dispersion of the projectile fragments instead of the r.m.s. thermal expansion velocity of a charge cloud.

The velocity (momentum) dispersion of projectile fragments has been studied for several projectile particles and energies.[22-24] The parallel momentum dispersion has been fit by the general expression

$$\left\langle p^2 - \langle p \rangle^2 \right\rangle^{1/2} = \sigma_0 \sqrt{\frac{A_F(A-A_F)}{A-1}} \tag{6}$$

where A is the mass of the projectile and $A_F$ the mass of the fragment. Table V lists the values of $\sigma_0$ for the systems studied in ref. 22-24. We assume the constant 86 MeV/c for our work. The parameter $\beta_T$ used in our fitting procedure was calculated using an expression of the same form as equation 6. Specifically, we assumed

$$\beta_T = \frac{0.16}{A_F}\sqrt{\frac{A_F(A-A_F)}{A-1}} \quad . \tag{7}$$

where $0.16 = \sqrt{3}\sigma_0/931.5$ MeV. The factor $\sqrt{3}$ was obtained by assuming that the momentum dispersion of the two components perpendicular to the beam was the same as the parallel dispersion, then adding the three components in quadrature. The mass numbers in this equation were calculated from the charges by assuming that the charge-to-mass ratios of the projectile and target fragments were the same as the original nuclei.

Even clearer evidence that the pion focusing or defocusing near beam velocity is associated with bound fragments comes from the downshift of the peaks. For the $^{20}$Ne beam the $\pi^-$ peak is consistently downshifted from beam velocity by 3.2 ± 1.6 MeV/c (projectile frame). The $\pi^+$ depression downshift is less well defined but is about the same as $\pi^-$. Van Bibber et al.[24] state that the mean energy of fragments is downshifted by about 10 MeV per nucleon, which is equivalent to pion momentum shift in the projectile frame of 3.4 MeV/c. Greiner et al.[22] measured the momentum shifts of the beam fragments at higher beam energies where they are about a factor of 3 smaller than the shift measured by Van Bibber et al. Our data at intermediate bombarding energies lie closer to the shifts measured at the lower beam energies.

Van Bibber et al.[24] show that the momentum dispersion perpendicular to the beam exceeds the parallel dispersion at their energies, and this feature is attributed to orbital deflection. This anisotropy is expected to decrease with increasing bombarding energy, and Greiner et al.[22] specifically state the dispersion is isotropic within 10% at 1 and 2 GeV/N. The fits shown on Figs. 2-17 have assumed that the momentum dispersion of the beam fragments is isotropic. However, a careful

examination of some of our figures indicates a slight anisotropy in that the width in the perpendicular direction slightly exceeds that in the parallel direction. A more quantitative measure of the systematic sideward anisotropy of the beam velocity $\pi^-$ peak is seen in Table III by comparison of the half widths $_i/2$, corrected for experimental resolution. This anisotropy is most pronounced for the lowest energy (E/A = 280 MeV) Ne data and for the Ar data. That the $\pi^-$ peak anisotropy qualitatively follows the projectile fragment anisotropy is further evidence that the Coulomb focusing by projectile fragments governs the $\pi^-$ peak.

The effective projectile fragment Z values of Table IV and Fig. 19 show a slight decrease with bombarding energy for the lighter targets, reversing for heavy targets. For the nearly equal mass Ne-NaF collisions, the Z values for $\pi^-$ are typically about half the initial charge of the neon beam, while the values for $\pi^+$ are more nearly a third of the initial charge. As the mass of the target increases, the effective Z value consistently decreases for both $\pi^+$ and $\pi^-$. For the neon beam the effective charge on the projectile fragment for $\pi^+$ is less than for $\pi^-$ for all targets which were used. This difference is qualitatively understood in that a beam velocity $\pi^+$ arises from a smaller average inpact parameter than $\pi^-$, as noted by GK.[10] This difference between $\pi^+$ and $\pi^-$ is not seen for the argon beam. However, the fitting procedure has not been as successful for argon as for neon projectiles. The peak in the fit to the $\pi^-$ spectrum is not as sharp as the data and the depression in the fit to the $\pi^+$ spectrum is too sharp.

The values of the normalization parameter in the uncharged pion source function (N in eq. 4) found by the fitting procedure are given in

Table IV. As in the fireball model,[21] these values of N are almost independent of beam energy, suggesting that it is just a geometric factor. To illustrate the beam energy dependence of eq. (4) and to display it in a manner independent of the parameters $c_1$ and $c_2$, fig. 20 shows the values of the Lorentz invariant form of the uncharged pion source function ($Ed^3\sigma/dp^3$) evaluated for pions at rest in the center of mass [$N' \equiv m_\pi \sigma_o(p_{CM} = 0) = Nm_\pi \exp(-m_\pi/T)$] vs the kinetic energy per nucleon of the beam in the center of mass ($E^*$). Since N is nearly independent of beam energy, the beam energy dependence of N' is contained in the Boltzmann factor $\exp(-m_\pi/T)$. We have found that the values of N' can be parameterized by the simple semi-empirical expression

$$N'_\pm = N_o Y_\pm \exp(E^*/B) \qquad (8)$$

where

$$Y_+ = \pi r_o^2 (Z_p A_t^{2/3} + Z_t A_p^{2/3})$$

$$Y_- = \pi r_o^2 (N_p A_t^{2/3} + N_t A_p^{2/3})$$

and

$A_t, Z_t, N_t$ = number of nucleons, protons, neutrons in the target,

$A_p, Z_p, N_p$ = number of nucleons, protons, neutrons in the projectile.

The geometric factor Y is discussed and described elsewhere[1,21,26-27]. Using eq. (8) with $r_o = 1.2$ fm, $N_o = (616\ \text{MeV/c})^{-3}$ and $B = 33$ MeV, the lines shown in fig. 20 can be calculated. The lines fit reasonably all the points except the $Ne + U \rightarrow \pi^+$ data.

The values of $c_1$, which are related to the departure of the source function (eq. 4) from a Boltzmann distribution, consistently decrease with increasing target mass and with increasing beam energy. Because the

calculated cross section can be negative for $c_1$ less than zero, we have restricted it to positive values. When $c_2$ is zero, the source function is isotropic in the center of mass. A positive value of $c_2$ indicates a source function that is forward-backward peaked in the center of mass. We have restricted $c_2$ to positive values to avoid sideward peaking of the source function and because the calculated cross section can be negative for $c_2$ less than zero. The fitted values of $c_2$ are generally consistent with zero, but they are poorly determined since our data are concentrated at low center of mass angles.

Some of the failures in the fitting procedure are probably due to the use of a single value for the projectile fragment charge. An implicit assumption involved in the fitting is that after impact parameter averaging the Coulomb effects can be represented by functions for some average impact parameter. The observed charged pion spectra arise from an impact parameter averaging in which the fragment yield falls off monotonically below the projectile Z, but the probability of pion production must rise with the decreasing projectile fragment charge (i.e., more central collisions). We have replaced this averaging procedure with a function of a single effective charge. This approximation seems to fail for the argon beam. With the detailed averaging procedure of ref. 25 satisfactory fits are obtained for both Ne + C and Ar + C systems.

## V. Conclusions

In summary, strong Coulomb effects on the charged pion spectra are observed near the beam velocity and, by inference, near the target velocity. For light target-projectile combinations, these effects can be explained quantitatively in terms of Coulomb interactions between the

pions and cold projectile fragments using Gyulassy and Kauffmann's[10] Coulomb correction formulas. Our treatment of the Coulomb effects differs from that of Gyulassy and Kauffmann in that a different expression has been used for the uncharged pion source function (see eq. 4). We also reinterpret their formulas for thermal averaging in terms of an average over the velocity dispersion of the projectile fragments. The shift of the peak in the $\pi^-$ spectra from the incident beam velocity and the approximate width of these peaks are consistent with previously measured projectile fragmentation data[22-24]. We have also seen that the effective charge of the projectile fragment is less for $\pi^+$ near beam velocity than for $\pi^-$. This difference is consistent with our expectation that positive pions near beam velocity tend to come from more central collisions. Using the same methods, qualitative agreement is achieved for heavier targets and projectiles. The differences between our fitting function and the data are due, at least in part, to an incomplete treatment of impact parameter averaging.

Our data cover a relatively small region of pion momenta and angles, but this band includes the region in which the Coulomb effects are expected to be greatest. In order to understand more exotic phenomena associated with the charged particle spectra in heavy ion interactions, these Coulomb effects must be understood in all momentum regions and taken into account.

Acknowledgements

Thanks are owed to P.J. Siemens and M. Gyulassy for useful suggestions and discussions, to Jeanne Hassenzahl for quick and accurate typing of the manuscript, and to the BEVALAC crew for preparation and tuning of the beams. This work was supported by the Director, Office of Energy Research, Division of Nuclear Physics of the Office of High Energy and Nuclear Physics of the U.S. Department of Energy under Contract W-7405-ENG-48, by the INS-LBL collaboration program, Institute for Nuclear Study, University of Tokyo, Japan, and by the U.S. National Science Foundation under grant No. 78-22696.

## Appendix I

The uncertainty associated with each parameter in Table IV was determined by calculating how much the parameter had to be changed, with all the other parameters freely adjustable, in order to increase the chi-squared ($\chi^2$) by one from its value at the minimum.[28] These errors are due to the statistical uncertainties in the data. They do not include uncertainties due to any systematic errors in the data or due to the assumptions involved in the fitting expression. Because the source shape parameters ($c_1$ and $c_2$ in eq. 4) for the $\pi^+$ fits were taken from the corresponding $\pi^-$ fits, the number of parameters that were varied during the complete error analysis was smaller for $\pi^+$ than for $\pi^-$.

As a result, the errors associated with the $\pi^+$ parameters are generally smaller than for $\pi^-$. The errors given for $c_1$ and $c_2$ are from the $\pi^-$ fit.

References

1. S. Nagamiya, M.-C. Lemaire, E. Moeller, S. Schnetzer, G. Shapiro, H. Steiner, I. Tanihata, LBL Report 12123 (1981) submitted to Phys. Rev. C..
2. J. Chiba, K. Nakai, I. Tanihata, S. Nagamiya, H. Bowman, J. Ingersoll, J.O. Rasmussen, Phys. Rev. C20, 1332 (1979).
3. J. Nakai, J. Chiba, I. Tanihata, M. Sasao, H. Bowman, S. Nagamiya, J.O. Rasmussen, Phys. Rev. C20, 2210 (1979).
4. K.L. Wolf, H.H. Gutbrod, W.G. Meyer, A.M. Poskanzer, A. Sandoval, R. Stock, J. Gosset, C.H. King, G. King, Nguyen Van Sen, G.D. Westfall, Phys. Rev. Lett. 42, 1448 (1979).
5. J. Papp, J. Jaros, L. Schroeder, J. Staples, H. Steiner, A. Wagner, J. Wiss, Phys. Rev. Lett. 34, 601 (1975); J. Papp, Ph.D. Thesis, LBL Report 3633 (1975).
6. S.Y. Fung, W. Gorn, G.P. Kiernan, F.F. Leu, J.J. Lu, Y.T. Oh, J. Osawa, R.T. Poe, L. Schroeder, H. Steiner, Phys. Rev. Lett. 40, 292 (1978).
7. W. Benenson, G. Bertsch, G.M. Crawley, E. Kashy, J.A. Nolen, Jr., H. Bowman, J.G. Ingersoll, J.O. Rasmussen, J. Sullivan, M. Koike, M. Sasao, J. Péter, T.E. Ward, Phys. Rev. Lett. 43, 683 (1979), 44, 54 (1980).
8. G. Bertsch, Nature 283, 280 (1980).
9. K.G. Libbrecht and S.E. Koonin, Phys. Rev. Lett. 43, 1581 (1979).
10. M. Gyulassy and S.K. Kauffmann, Nucl. Phys. A362, 503 (1981).
11. C.M. Ko and P.J. Siemens, Nucl. Phys. A (in press).
12. E.M. Friedländer, Phys. Lett. 2, 38 (1962).

13. N.I. Kostanashvili, G.I. Lebedevich, D.S. Nabichvrishvili, Yad. Fiz. 13, 1243 (1971) [Sov. J. Nucl. Phys. 13, 715 (1971)].

14. J. Burfening, E. Gardner, C.M.G. Lattes, Phys. Rev. 75, 382 (1949).

15. H. Yagoda, Phys. Rev. 85, 891 (1952).

16. J.C. Alder, B. Gabioud, C. Joseph, J.F. Loude, N. Morel, A. Perrenoud, M.T. Tran, B. Vaucher, E. Winkelmann, D. Renker, H. Schmitt, C. Zupancic, H. Von Fellenberg, A. Frischknecht, F. Hoop, G. Strassner, P. Truöl, Nucl. Instr. and Meth. 160, 93 (1979).

17. A.S. Carroll, I.H. Chiang, C.B. Dover, T.F. Kycia, K.K. Li, P.O. Mazur, D.N. Michael, P.M. Mockett, D.C. Rahm, R. Rubenstein, Phys. Rev. C14, 635 (1976).

18. K. Frankel, J. Bistirlich, H. Bowman, R. Bossingham, K.M. Crowe, C.J. Martoff, D. Murphy, J. Rasmussen, J. Sullivan, W. Zajc, O. Hashimoto, M. Koike, J. Peter, W. Benenson, G.M. Crawley, E. Kashy, J.A. Nolen, Jr., LBL report 12585 (1981), to be published.

19. R. Wada and J.R. Alonso, IEEE Trans. Nucl. Science NS-28, 2276 (1981).

20. J.P. Sullivan, Ph.D. Thesis, University of California, Berkeley, LBL-12546 (1981) unpublished.

21. J.I. Kapusta, Phys. Rev. C16, 1493 (1977).

22. D.E. Greiner, P.J. Lindstrom, H.H. Heckman, Bruce Cork, F.S. Bieser, Phys. Rev. Lett. 35, 152 (1975).

23. Y.P. Viyogi, T.J.M. Symons, P. Doll, D.E. Greiner, H.H. Heckman, D.L. Hendrie, P.J. Lindstrom, J. Mahoney, D.K. Scott, K. Van Bibber, G.D. Westfall, H. Wieman, H.J. Crawford, C. McParland, C.K. Gelbke, Phys. Rev. Lett. 42, 33 (1979).

24. K. Van Bibber, D.L. Hendrie, D.K. Scott, H. H. Wieman, L.S. Schroeder, J.V. Geaga, S.A. Chessin, R. Treuhaft, Y.J. Grossiord, J.O. Rasmussen, C.Y. Wong, Phys. Rev. Lett. 43, 840 (1979).

25. H.M.A. Radi, J.O. Rasmussen, J.P. Sullivan, K.A. Frankel, O. Hashimoto, LBL report 12591 (1981) (to be published).

26. R.J. Glauber and G. Matthiae, Nucl. Phys. B21, 135 (1970).

27. J. Hufner and J. Knoll, Nucl. Phys. A290, 460 (1977).

28. Both the fitting and the error analysis were done with the MINUIT program (version 2.77) written at CERN. A description of this program, the minimization methods used (see the section on MIGRAD), and the error analysis (see the section on MINOS) are available from: Program Library, Division DD, CERN, CH 1211 Geneve 23, Switzerland. Ask for the long writeup on MINUIT, D506.

TABLE I

Normalization and Correction Factors and Their Uncertainties

| Factor | Typical Value | Estimated Uncertainty[f] |
|---|---|---|
| Beam intensity | | ±25 |
| Computer dead time | 20 | ± 5 |
| MWPC inefficiency | 5–10 | ± 3 |
| Events rejected because they did not trace back to the target[a] | 20 | ± 6 |
| dE/dx cuts[b] | 5–10 | ± 3 |
| Range cuts[c] | 15–40 | ±10 |
| Spectrometer acceptance[d] | | ±10 |
| Overall uncertainty[e] | | ±30 |

a. These events were rejected because the trajectory did not trace back to the target; many of the muons from decay in flight of pions are rejected by this cut.

b. Cuts on the energy loss (dE/dx) in the first two scintillators.

c. Cuts on the range of the particle in the scintillator stack.

d. This includes uncertainties in the calculation itself, in the field map, and in the target and detector positions.

e. Calculated by combining all uncertainties in quadrature.

f. The estimated uncertainty in the overal normalization due to the factor e.g. computer dead time correction was 20% ± 5%.

Table II
Summary of Experimental Parameters

| Beam | Beam Energy Per Nucleon (MeV) at Accelerator | Beam Energy Per Nucleon (MeV) at Center of Target[a] | Target Material | Target Thickness ($g/cm^2$) | Pion Momentum with Velocity of Incident Beam (MeV/c) | Resolution[b] $\sigma_p$ (%) | Resolution[b] $\sigma_\theta$ (deg) |
|---|---|---|---|---|---|---|---|
| $^{20}Ne$ | 300 | 280 | C | 0.56 | 116 | 2.2 | 2.0 |
| | | 281 | NaF | 0.60 | 116 | 2.2 | 2.1 |
| | | 282 | Cu | 0.45 | 117 | 2.3 | 2.4 |
| $^{20}Ne$ | 400 | 380 | NaF | 1.07 | 138 | 2.1 | 2.2 |
| | | 382 | Cu | 0.91 | 139 | 2.0 | 2.6 |
| | | 385 | U | 0.52 | 139 | 2.2 | 2.9 |
| $^{20}Ne$ | 500 | 482 | C | 1.12 | 159 | 1.5 | 1.9 |
| | | 483 | NaF | 1.07 | 160 | 1.4 | 2.0 |
| | | 485 | Cu | 0.91 | 160 | 1.9 | 2.9 |
| | | 487 | U | 0.52 | 160 | 1.6 | 2.4 |
| $^{40}Ar$ | 557 | 533 | C | 0.56 | 169 | 1.4 | 1.7 |
| | | 534 | KCl | 0.50 | 170 | 1.4 | 1.8 |

a. The beam energy at the center of the target is less than the energy at the exit of the accelerator due to energy loss in material in the beam line as well as energy loss in the target. These beam energies were measured as described in reference 19.

b. The resolution is defined as the r.m.s. difference between the calculated momentum or angle and the true value.

TABLE III

Widths and Momentum Shifts of Peaks in $\pi^-$ Spectra

| $E_{beam}/A$ (MeV) | Beam | Target | $dp_{\parallel}$ [a] (MeV/c) | $\Gamma_{\parallel}/2$ [b] (MeV/c) | $\Gamma_{\perp}/2$ [c] (MeV/c) |
|---|---|---|---|---|---|
| 280 | $^{20}Ne$ | C | 3.0 | 7 | 10 |
| 281 | $^{20}Ne$ | NaF | 3.5 | 8 | 10 |
| 282 | $^{20}Ne$ | Cu | 4.0 | 9 | 13 |
| 380 | $^{20}Ne$ | NaF | 3.5 | 9 | 8 |
| 382 | $^{20}Ne$ | Cu | 3.5 | 11 | 11 |
| 385 | $^{20}Ne$ | U | 3.5 | 12 | 10 |
| 482 | $^{20}Ne$ | C | 3.0 | 8 | 10 |
| 483 | $^{20}Ne$ | NaF | 3.0 | 8 | 10 |
| 485 | $^{20}Ne$ | Cu | 2.5 | 9 | 10 |
| 487 | $^{20}Ne$ | U | 2.5 | 13 | 13 |
| 533 | $^{40}Ar$ | C | 2.5 | 5 | 7 |
| 534 | $^{40}Ar$ | KCl | 1.5 | 6 | 11 |

a. Shift of the center of the peak in the $\pi^-$ spectrum from the incident beam velocity, measured in the beam velocity reference frame.

b. Half-width at half maximum (measured from a smooth background) of the peak in the $\pi^-$ spectrum in the $p_{\parallel}$ direction, corrected for experimental resolution. Measured in the beam velocity reference frame.

c. Half-width at half maximum (measured from a smooth background) of the peak in the $\pi^-$ spectrum in the $p_{\perp}$ direction, corrected for experimental resolution.

Table IV

Parameters from Least Square Fitting of Pion Data

| $E_{beam}$ (MeV/A) | Beam | Target | $Z_{eff}$[a] $\pi^+$ | $Z_{eff}$[a] $\pi^-$ | $N$[b] $\frac{\mu b}{MeV^3}$ $\pi^+$ | $N$[b] $\frac{\mu b}{MeV^3}$ $\pi^-$ | $\sigma_{tot}$[c] (mb) $\pi^+$ | $\sigma_{tot}$[c] (mb) $\pi^-$ | T[d] (MeV) | $c_1$[e] | $c_2$[e] | $\chi^2/N$[f] $\pi^+$ | $\chi^2/N$[f] $\pi^-$ |
|---|---|---|---|---|---|---|---|---|---|---|---|---|---|
| 280 | $^{20}Ne$ | C | 3.8 ± 0.2 | 6.4 ± 0.2 | 0.11 ± 0.01 | 0.11 ± 0.01 | 25 | 25 | 30 | 2.9 ± 0.5 | 0. ± 0.4 | 2.06 | 1.74 |
| 281 | $^{20}Ne$ | NaF | 3.1 ± 0.2 | 5.6 ± 0.2 | 0.16 ± 0.01 | 0.19 ± 0.01 | 30 | 35 | 30 | 2.1 ± 0.6 | 1.0 ± 0.5 | 1.33 | 2.00 |
| 282 | $^{20}Ne$ | Cu | 1.8 ± 0.3 | 4.3 ± 0.3 | 0.40 ± 0.02 | 0.47 ± 0.04 | 58 | 69 | 30 | 1.4 ± 0.7 | 1.3 ± 0.7 | 1.12 | 1.64 |
| 380 | $^{20}Ne$ | NaF | 3.3 ± 0.1 | 4.6 ± 0.1 | 0.15 ± 0.01 | 0.15 ± 0.01 | 85 | 113 | 36 | 1.7 ± 0.1 | 0.0 ± 0.1 | 2.28 | 2.63 |
| 382 | $^{20}Ne$ | Cu | 2.3 ± 0.1 | 3.4 ± 0.1 | 0.37 ± 0.01 | 0.37 ± 0.02 | 169 | 194 | 36 | 1.1 ± 0.2 | 0.0 ± 0.1 | 1.29 | 1.58 |
| 385 | $^{20}Ne$ | U | 1.5 ± 0.3 | 2.7 ± 0.2 | 0.91 ± 0.04 | 1.62 ± 0.15 | 292 | 521 | 36 | 0.6 ± 0.2 | 0.0 ± 0.1 | 0.94 | 1.47 |
| 482 | $^{20}Ne$ | C | 3.5 ± 0.1 | 5.0 ± 0.1 | 0.08 ± 0.01 | 0.09 ± 0.01 | 149 | 155 | 45 | 1.1 ± 0.2 | 0.0 ± 0.1 | 2.10 | 1.44 |
| 483 | $^{20}Ne$ | NaF | 2.9 ± 0.1 | 4.4 ± 1.8 | 0.14 ± 0.01 | 0.16 ± 0.01 | 217 | 243 | 45 | 0.8 ± 0.1 | 0.0 ± 0.1 | 1.86 | 2.16 |
| 485 | $^{20}Ne$ | Cu | 2.2 ± 0.1 | 3.5 ± 0.1 | 0.31 ± 0.01 | 0.43 ± 0.01 | 184 | 253 | 45 | 0. ± 0.1 | 0.2 ± 0.1 | 2.38 | 2.06 |
| 487 | $^{20}Ne$ | U | 1.8 ± 0.3 | 3.1 ± 0.2 | 0.63 ± 0.03 | 1.54 ± 0.04 | 374 | 913 | 45 | 0. ± 0.1 | 0.0 ± 0.1 | 1.17 | 1.02 |
| 533 | $^{40}Ar$ | C | 8.4 ± 0.4 | 6.3 ± 0.1 | 0.12 ± 0.01 | 0.16 ± 0.01 | 300 | 420 | 50 | 0.7 ± 0.1 | 0.0 ± 0.1 | 2.73 | 2.36 |
| 534 | $^{40}Ar$ | KCl | 4.2 ± 0.3 | 4.4 ± 0.2 | 0.27 ± 0.01 | 0.44 ± 0.01 | 339 | 558 | 50 | 0.1 ± 0.1 | 0.0 ± 0.1 | 1.76 | 1.42 |

TABLE IV (continued)

a. Effective charge of projectile fragment

b. Normalization parameter in equation 4

c. The uncharged pion source function integrated over all momenta and angles. Notice that the source function is symmetric about the center of mass, so this is not a good measure of the total cross section except for equal mass collisions. In the asymmetric cases, this is still given in order to put the normalization in familiar units.

$$\sigma_{tot} = 4\pi N m_\pi^3 \left(\frac{T}{m_\pi}\right)\left\{K_2\left(\frac{m_\pi}{T}\right) + \frac{3c_1 T}{m_\pi} K_3\left(\frac{m_\pi}{T}\right)\right\}$$

where $K_2$ and $K_3$ are modified Bessel functions and the other parameters are defined as in equation 4.

d. The temperature in the Boltzmann factor of the uncharged pion source function (eq. 4). Estimated from the data of Ref. 1.

e. $c_1$, $c_2$ = source shape parameters in equation 4. A zero value means less than $10^{-5}$.

f. $\chi^2/N$ = chi-squared per degree of freedom in the fit. The number of degrees of freedom for a given set of data ranges from 39 to 126, with an average of 70.

TABLE V

Momentum Dispersion of Projectile Fragments

| Authors | E/A MeV | Beam | Target | $\sigma_o$ MeV/c |
|---|---|---|---|---|
| Greiner et al[22] | 1050 | $^{12}C$ | various[a] | 70 ± 2[b] |
| | 2100 | $^{12}C$ | various[a] | 74 ± 2[b] |
| | 2100 | $^{16}O$ | various[a] | 86 ± 2[b] |
| Viyogi et al[23] | 213 | $^{40}Ar$ | C | 94 ± 5 |
| Van Bibber | 92.5 | $^{16}O$ | Al | 86 |
| et al[24] | 92.5 | $^{16}O$ | Au | 80 |

a. Averaged over targets from Be to Pb. The authors say that $\sigma_o$ does not depend on target mass above the 5% level.

b. Notice that their definition of $\sigma_o$ differs from our definition by a factor of 2; the values of $\sigma_o$ quoted here are one-half of the values given in the original reference.

Figure captions:

Fig. 1. Schematic diagram of the apparatus

Fig. 2. Lorentz invariant cross section cuts for Ne + NaF → $\pi^{\pm}$ at E/A = 281 MeV. The left side of the graph shows the cross section vs momentum at 0 degrees in the lab for $\pi^-$ (top) and $\pi^+$ (bottom). The right side shows the cross section vs lab angle at a fixed lab momentum near the peak in the $\pi^-$ spectrum. The solid line is from a least squares fit of a function based on the Coulomb correction equations of Gyulassy and Kauffmann[10]. This solid line has the experimental resolution folded into it. The dashed line is the same function before folding with the resolution. The dotted line shows the cross section predicted by the uncharged pion source function to which the Coulomb corrections were applied. The arrows on the left-hand graphs mark the velocity of the incident beam.

Fig. 3. Lorentz invariant cross section cuts for Ne + NaF → $\pi^{\pm}$ at E/A = 380 MeV. See also the caption for figure 2.

Fig. 4. Lorentz invariant cross section cuts for Ne + NaF → $\pi^{\pm}$ at E/A = 483 MeV. See also the caption for figure 2.

Fig. 5. Lorentz invariant cross section cuts for Ar + KCl → $\pi^{\pm}$ at E/A = 534 MeV. See also the caption for figure 2.

Fig. 6A. Lorentz invariant cross section vs lab momentum for Ne + C → $\pi^-$ at E/A = 280 MeV. Each set of points is at a fixed lab angle, which is shown on the right side of the figure. A cross section offset has been added to the data at each angle (except the 20 degree data) in order to display it all on the same graph. This offset is given on the right side of the figure. The solid line is from a least squares fit of a function based on the Coulomb correction equations of Gyulassy and Kauffmann[10]. This function has been folded with the resolution of the spectrometer. The arrow marks the velocity of the incident beam.

Fig. 6B. Lorentz invariant cross section vs lab momentum for Ne + C → $\pi^+$ at E/A = 280 MeV. See also the caption for figure 6A.

Fig. 7A. Lorentz invariant cross section vs lab momentum for Ne + NaF → $\pi^-$ at E/A = 281 MeV. See also the caption for figure 6A.

Fig. 7B. Lorentz invariant cross section vs lab momentum for Ne + NaF → $\pi^-$ at E/A = 281 MeV. See also the caption for figure 6A.

Fig. 8A. Lorentz invariant cross section vs lab momentum for Ne + Cu → $\pi^-$ at E/A = 282 MeV. See also the caption for figure 6A.

Fig. 8B. Lorentz invariant cross section vs lab momentum for Ne + Cu → $\pi^+$ at E/A = 282 MeV. See also the caption for figure 6A.

Fig. 9A. Lorentz invariant cross section vs lab momentum for Ne + NaF → $\pi^-$ at E/A = 380 MeV. See also the caption for figure 6A.

Fig. 9B. Lorentz invariant cross section vs lab momentum for Ne + NaF → $\pi^+$ at E/A = 380 MeV. See also the caption for figure 6A.

Fig. 10A. Lorentz invariant cross section vs lab momentum for Ne + Cu → $\pi^-$ at E/A = 382 MeV. See also the caption for figure 6A.

Fig. 10B. Lorentz invariant cross section vs lab momentum for Ne + Cu → $\pi^+$ at E/A = 382 MeV. See also the caption for figure 6A.

Fig. 11A. Lorentz invariant cross section vs lab momentum for Ne + U → $\pi^-$ at E/A = 385 MeV. See also the caption for figure 6A.

Fig. 11B. Lorentz invariant cross section vs lab momentum for Ne + U → $\pi^+$ at E/A = 385 MeV. See also the caption for figure 6A.

Fig. 12A. Lorentz invariant cross section vs lab momentum for Ne + C → $\pi^-$ at E/A = 482 MeV. See also the caption for figure 6A.

Fig. 12B. Lorentz invariant cross section vs lab momentum for Ne + C → $\pi^+$ at E/A = 482 MeV. See also the caption for figure 6A.

Fig. 13A. Lorentz invariant cross section vs lab momentum for Ne + NaF → $\pi^-$ at E/A = 483 MeV. See also the caption for figure 6A.

Fig. 13B. Lorentz invariant cross section vs lab momentum for Ne + NaF → $\pi^+$ at E/A = 483 MeV. See also the caption for figure 6A.

Fig. 14A. Lorentz invariant cross section vs lab momentum for Ne + Cu → $\pi^-$ at E/A = 485 MeV. See also the caption for figure 6A.

Fig. 14B. Lorentz invariant cross section vs lab momentum for Ne + Cu → $\pi^+$ at E/A = 485 MeV. See also the caption for figure 6A.

Fig. 15A. Lorentz invariant cross section vs lab momentum for Ne + U → $\pi^-$ at E/A = 487 MeV. See also the caption for figure 6A.

Fig. 15B. Lorentz invariant cross section vs lab momentum for Ne + U → $\pi^+$ at E/A = 487 MeV. See also the caption for figure 6A.

Fig. 16A. Lorentz invariant cross section vs lab momentum for Ar + C → $\pi^-$ at E/A = 533 MeV. See also the caption for figure 6A.

Fig. 16B. Lorentz invariant cross section vs lab momentum for Ar + C → $\pi^+$ at E/A = 533 MeV. See also the caption for figure 6A.

Fig. 17A. Lorentz invariant cross section vs lab momentum for Ar + KCl → $\pi^-$ at E/A = 534 MeV. See also the caption for figure 6A.

Fig. 17B. Lorentz invariant cross section vs lab momentum for Ar + KCl → $\pi^+$ at E/A = 534 MeV. See also the caption for figure 6A.

Fig. 18. Contours of Lorentz invariant cross section $(E_\pi d^3\sigma/dp_\pi^3)$ on a rapidity $[y = \tanh^{-1}(p_{||}/E)]$ vs $p_\perp$ plot for Ne + NaF at E/A = 380 MeV. The present results have been combined with the data of Nakai et al[3] at larger angles to produce this plot. The cross sections from Nakai et al have been multiplied by a factor of 3/4 to correct for the difference between our normalization and theirs.

Fig. 19. Effective charge of the projectile fragment from the least squares fits of the Coulomb correction formulas[10] to the $\pi^-$ (top) and $\pi^+$ (bottom) data. The closed symbols are from the data with Ne beams and the open symbols with an Ar beam. The lines are to guide the eye. The target is shown next to each point or set of points.

Fig. 20. The values of the Lorentz invariant form of the uncharged pion source function (eq. 4) evaluated for pions at rest in the center of mass $[N' = m_\pi \sigma_o(p_{CM} = 0) = N m_\pi \exp(-m_\pi/T)]$ vs beam energy per nucleon in the center of mass. The closed symbols are for a Ne beam and the open symbols for an Ar beam. The lines are from a semi-empirical parameterization of these values (see eq. 8). The target is shown next to each point or set of points.

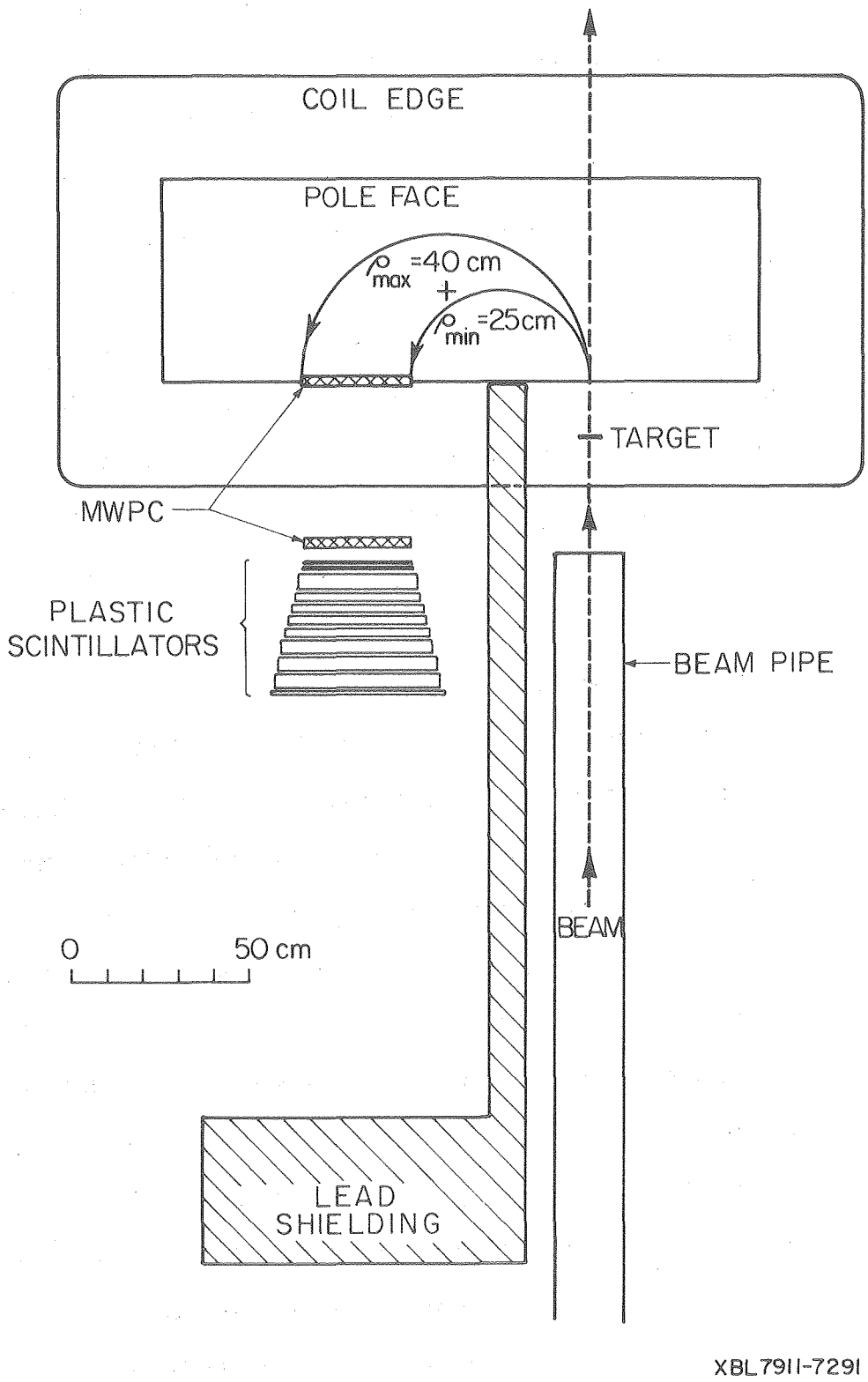
COIL EDGE
POLE FACE
$\rho_{max}$ =40 cm
+
$\rho_{min}$ =25cm
TARGET
MWPC
PLASTIC
SCINTILLATORS
BEAM PIPE
BEAM
0
50 cm
LEAD
SHIELDING
XBL7911-7291

Fig. 1

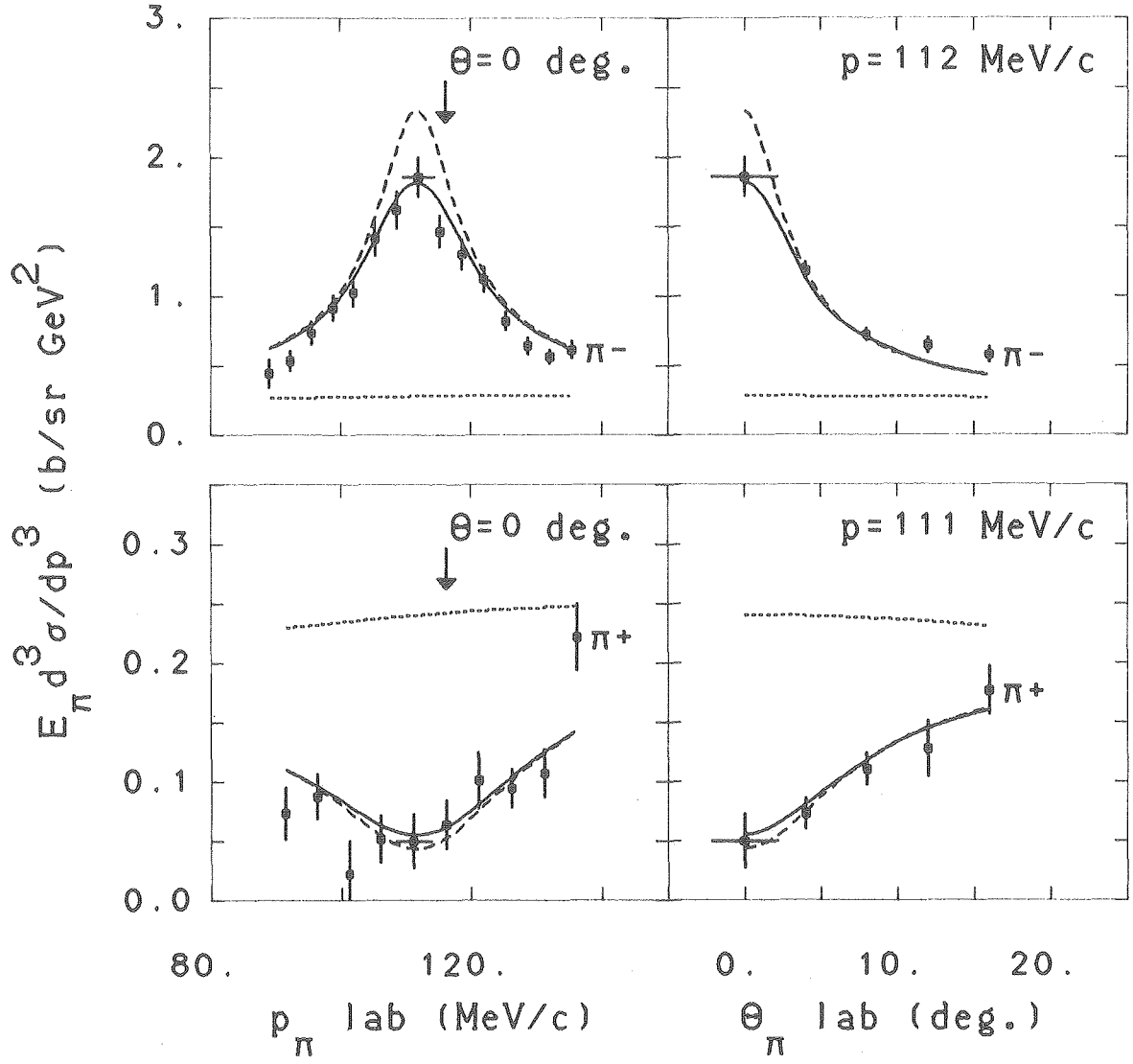
θ=0 deg.
p=112 MeV/c
π-
θ=0 deg.
p=111 MeV/c
π+
3.
2.
1.
0.
0.3
0.2
0.1
0.0
80.
120.
0.
10.
20.
$E_\pi d^3\sigma/dp^3$ (b/sr GeV$^2$)
$p_\pi$ lab (MeV/c)
$\theta_\pi$ lab (deg.)
XBL 816-10182

Fig. 2

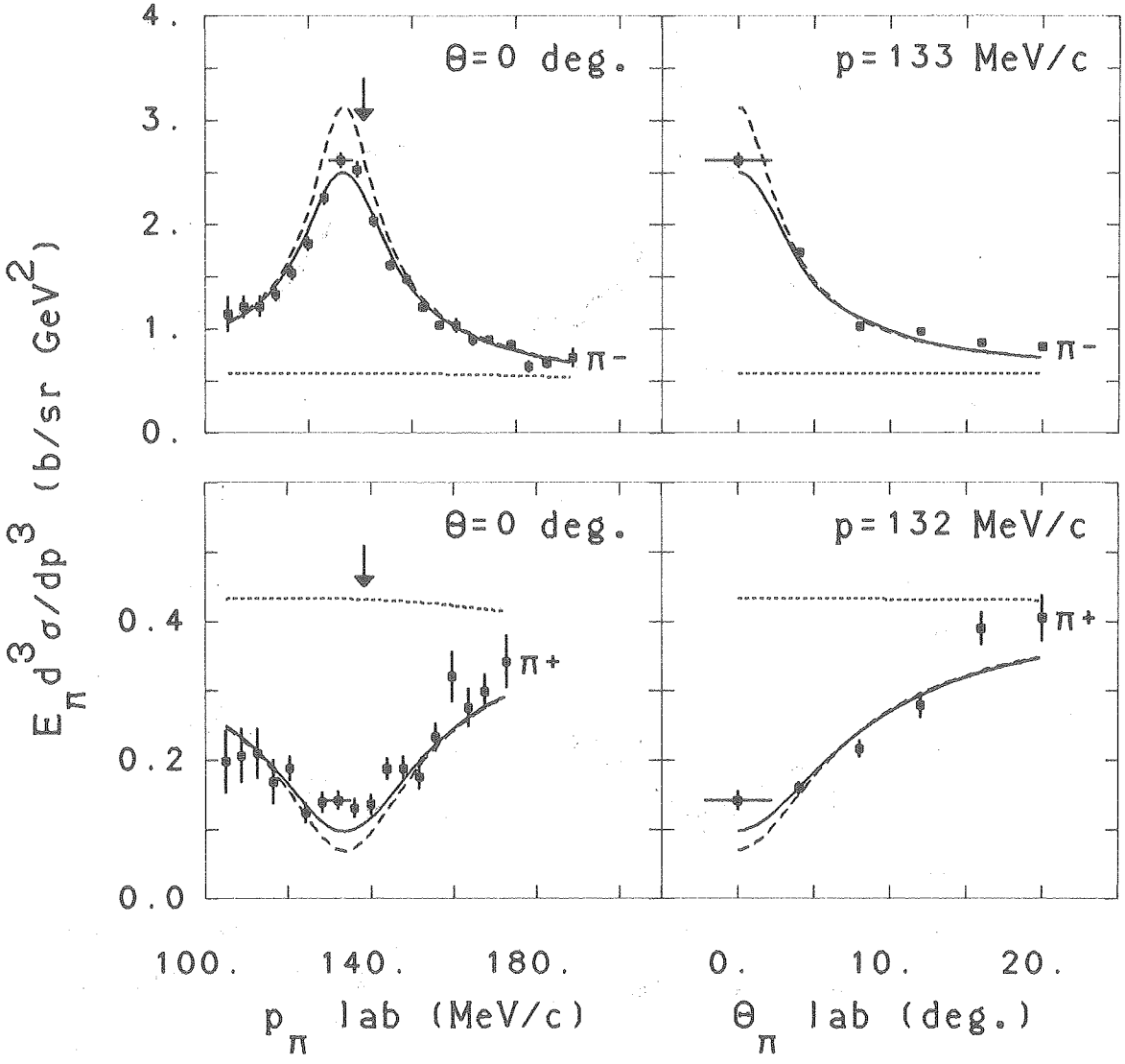
θ=0 deg.
p=133 MeV/c
π-
θ=0 deg.
p=132 MeV/c
π+
4.
3.
2.
1.
0.
0.4
0.2
0.0
100.
140.
180.
0.
10.
20.
$E_\pi d^3\sigma/dp^3$ (b/sr GeV$^2$)
$p_\pi$ lab (MeV/c)
$\theta_\pi$ lab (deg.)
XBL 816-10183

Fig. 3

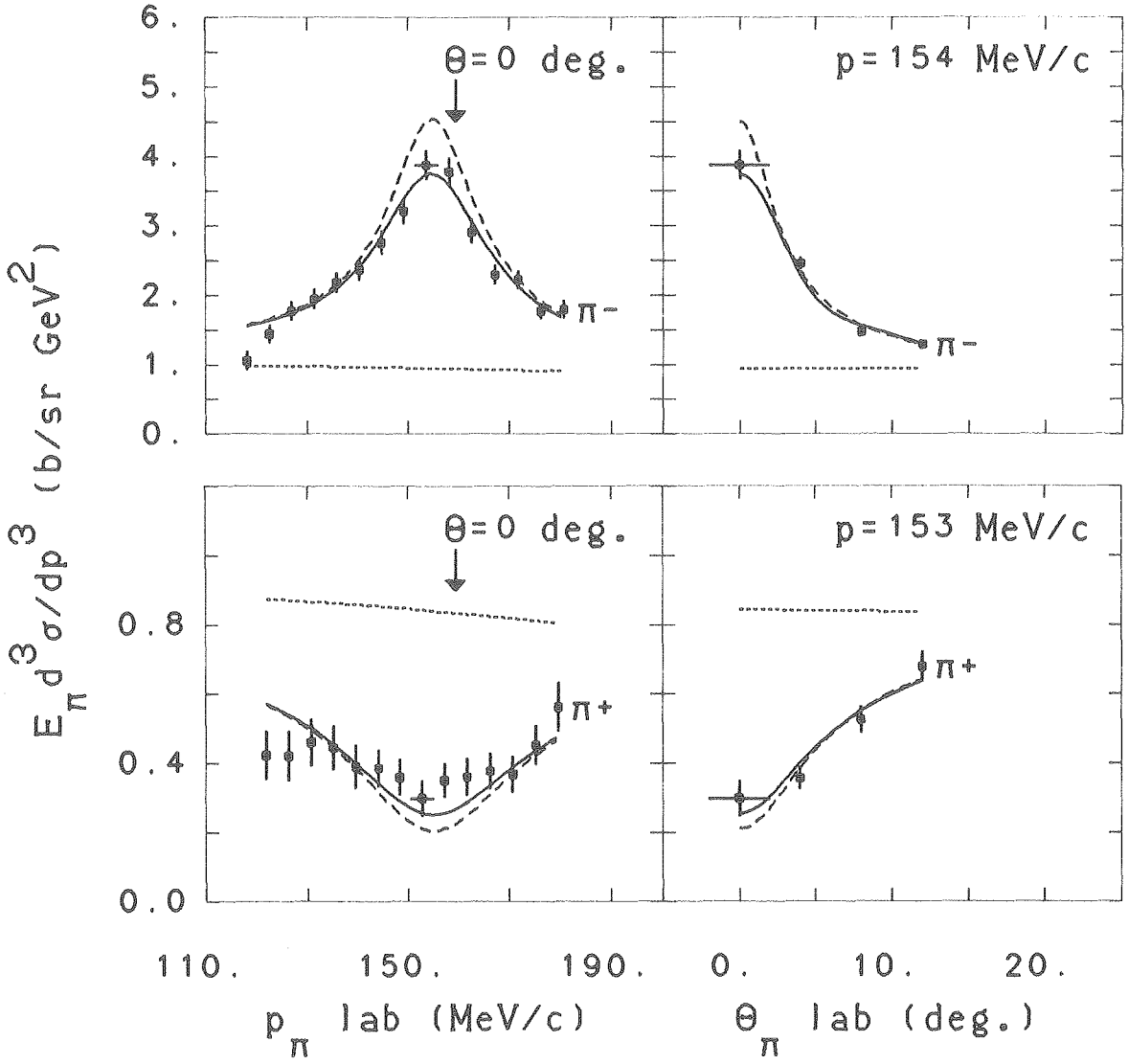


XBL 816-10184

Fig. 4

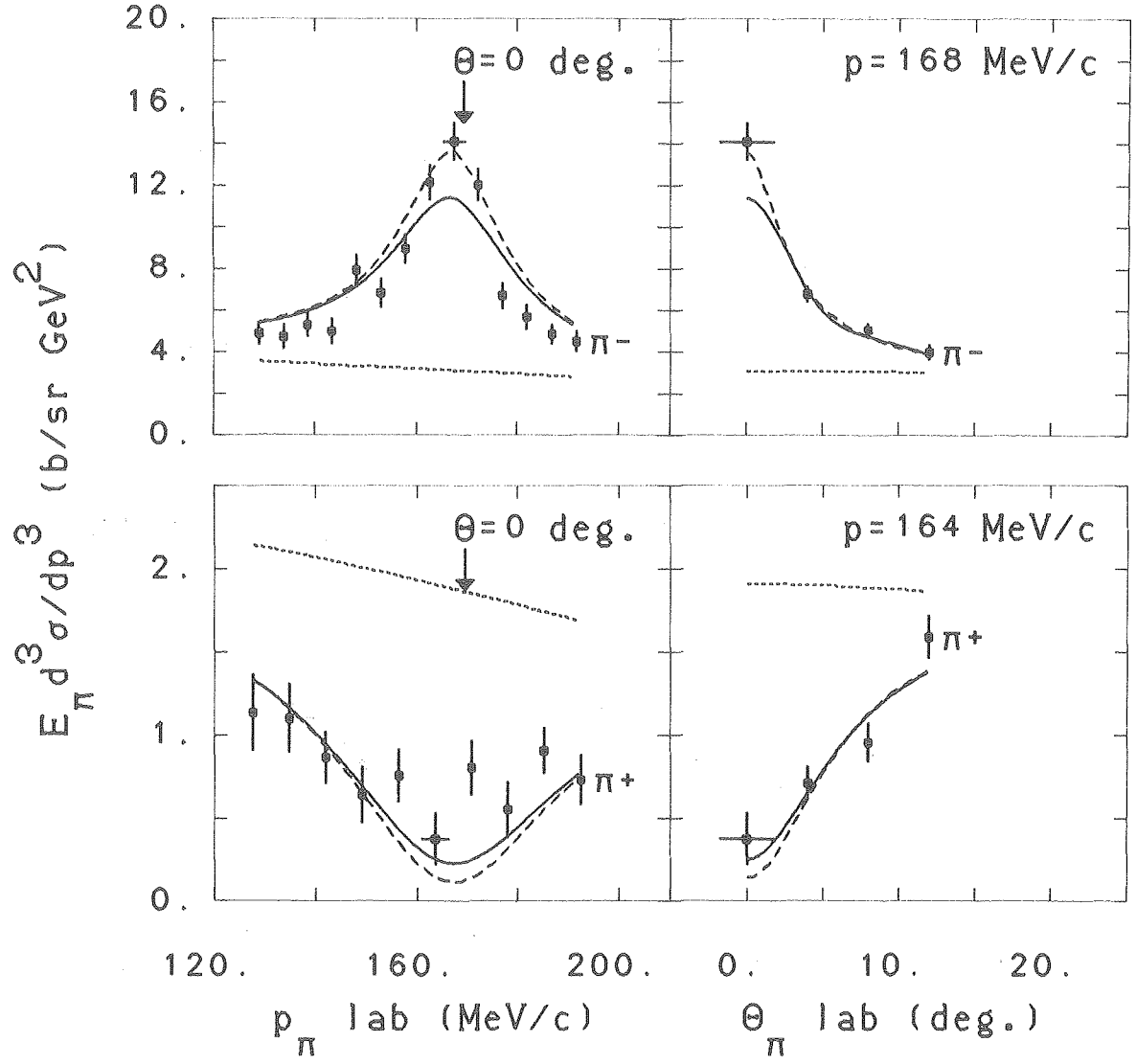


XBL 816-10186

Fig. 5

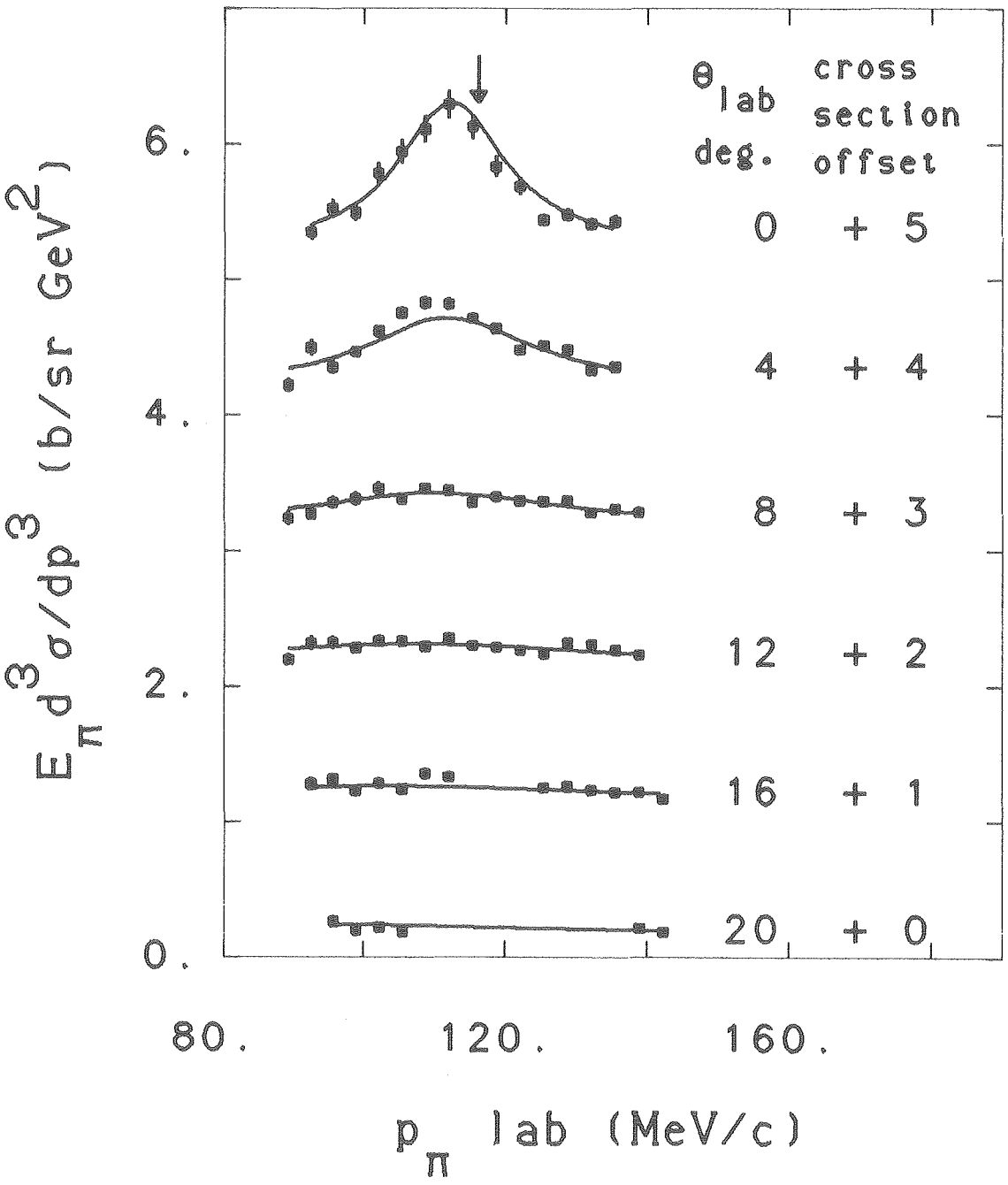
$E_\pi \frac{d^3\sigma}{dp^3}$ (b/sr GeV$^2$)
6.
4.
2.
0.
80.
120.
160.
$p_\pi$ lab (MeV/c)
$\theta_{lab}$ deg.
cross section offset
0 + 5
4 + 4
8 + 3
12 + 2
16 + 1
20 + 0
XBL 815-9938

Fig. 6A

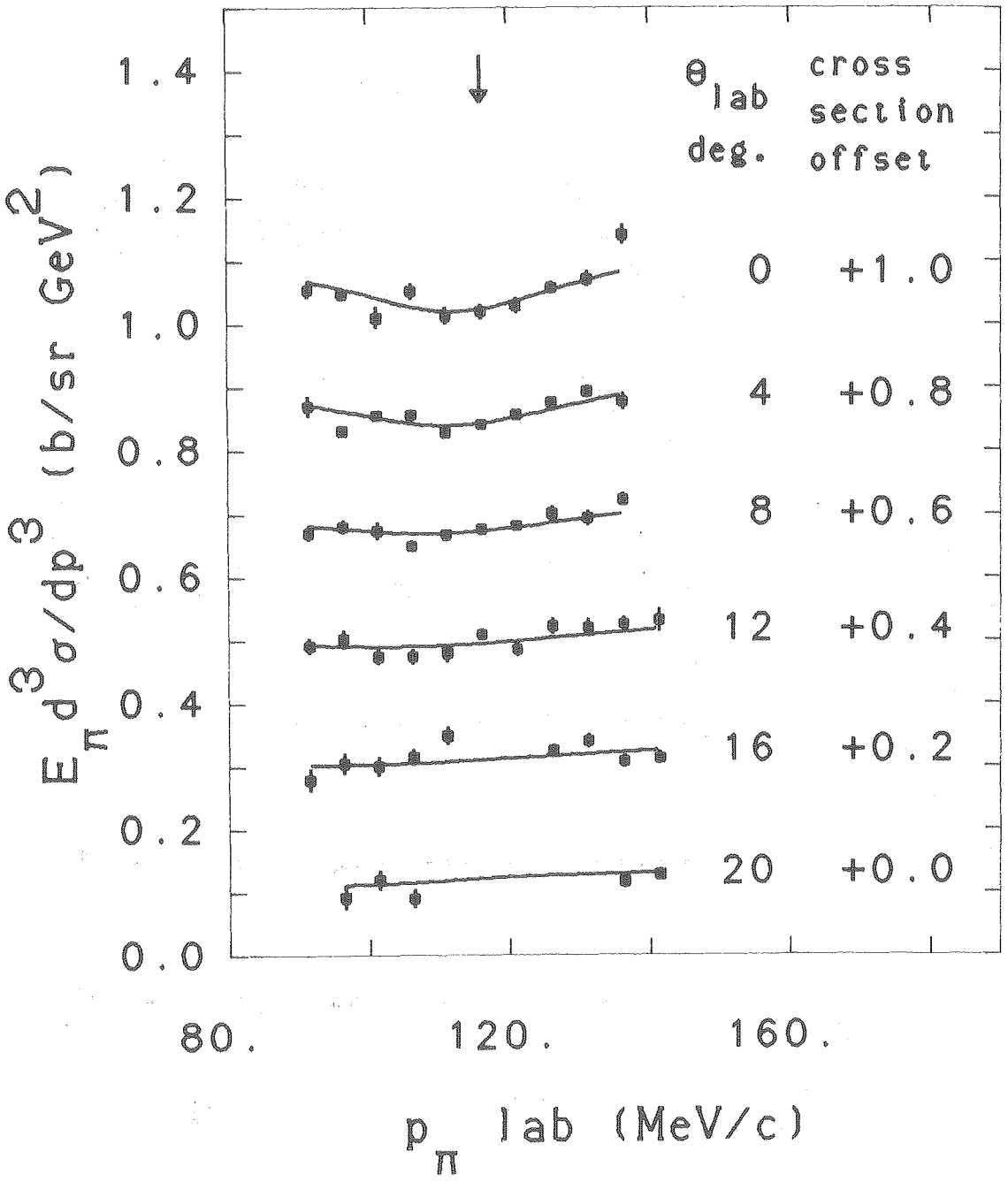
1.4
1.2
1.0
0.8
0.6
0.4
0.2
0.0
$E_\pi d^3\sigma/dp^3$ (b/sr GeV$^2$)
$\theta_{lab}$ deg.
cross section offset
0 +1.0
4 +0.8
8 +0.6
12 +0.4
16 +0.2
20 +0.0
80.
120.
160.
$p_\pi$ lab (MeV/c)
XBL 815-9941

Fig. 6B

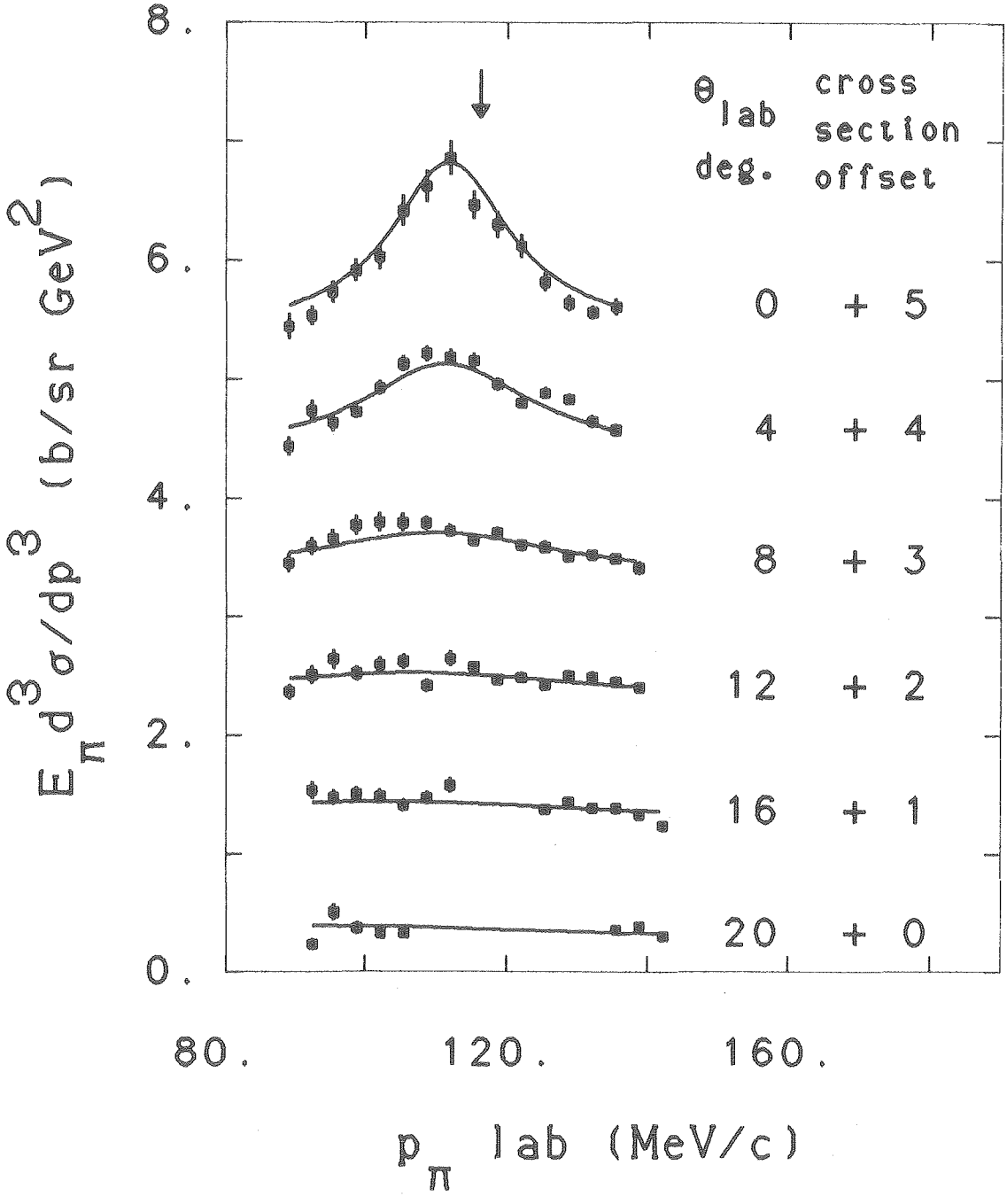


XBL 815-9939

Fig. 7A

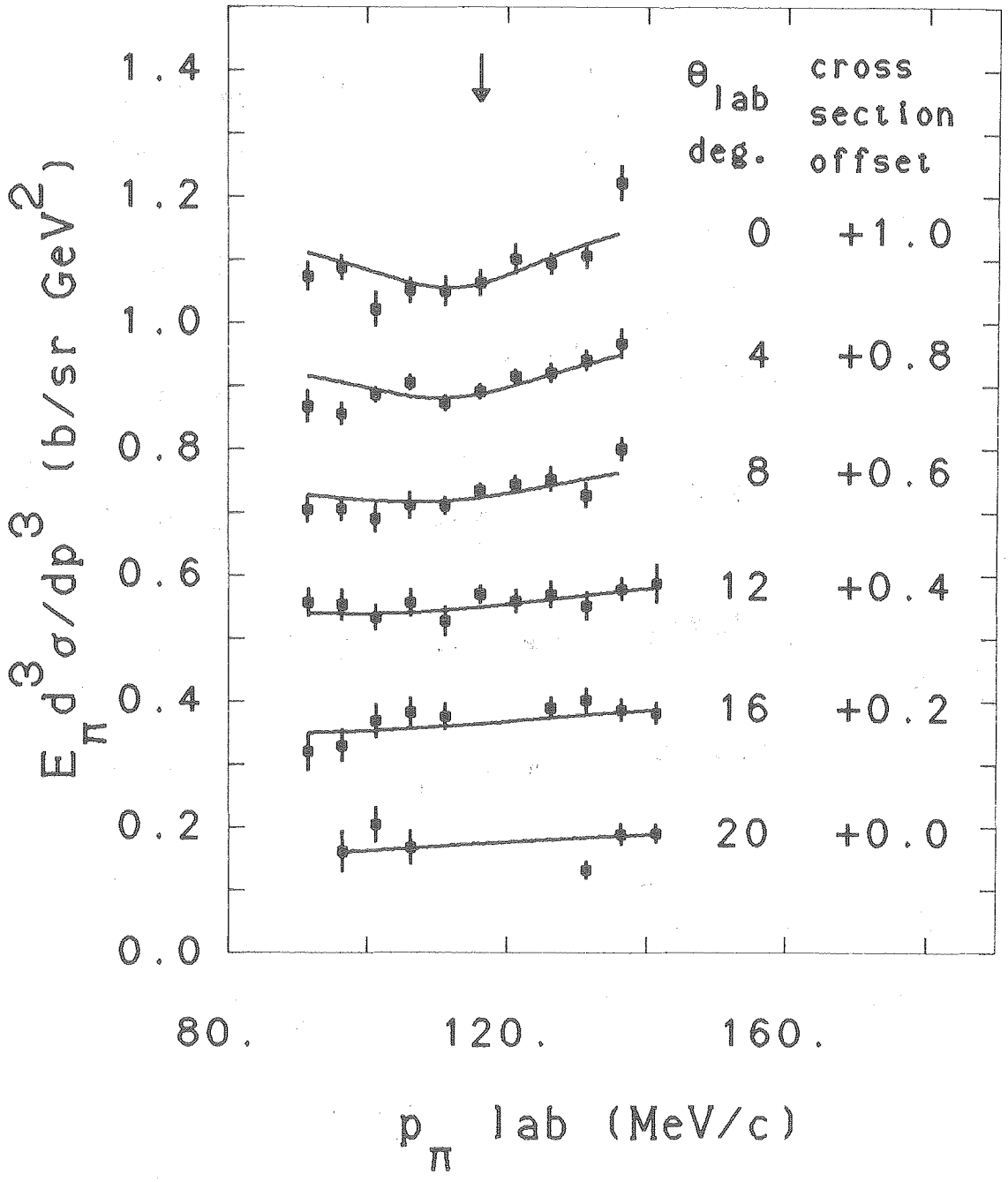


XBL 815-9942

Fig. 7B

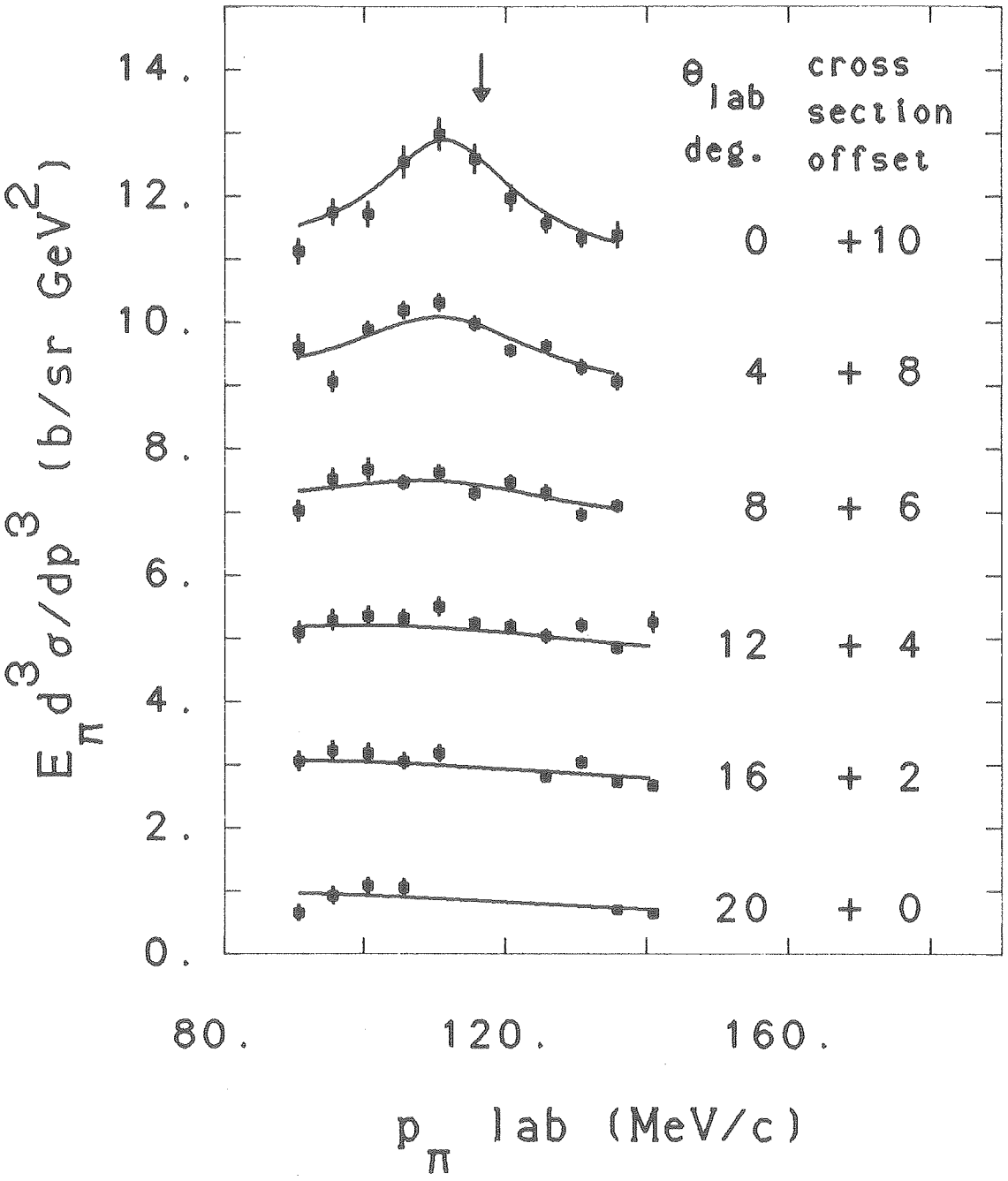
14.
12.
10.
8.
6.
4.
2.
0.
$E_\pi d^3\sigma/dp^3$ (b/sr GeV$^2$)
$\theta_{lab}$ deg.
cross section offset
0 +10
4 + 8
8 + 6
12 + 4
16 + 2
20 + 0
80.
120.
160.
$p_\pi$ lab (MeV/c)
XBL 815-9940

Fig. 8A

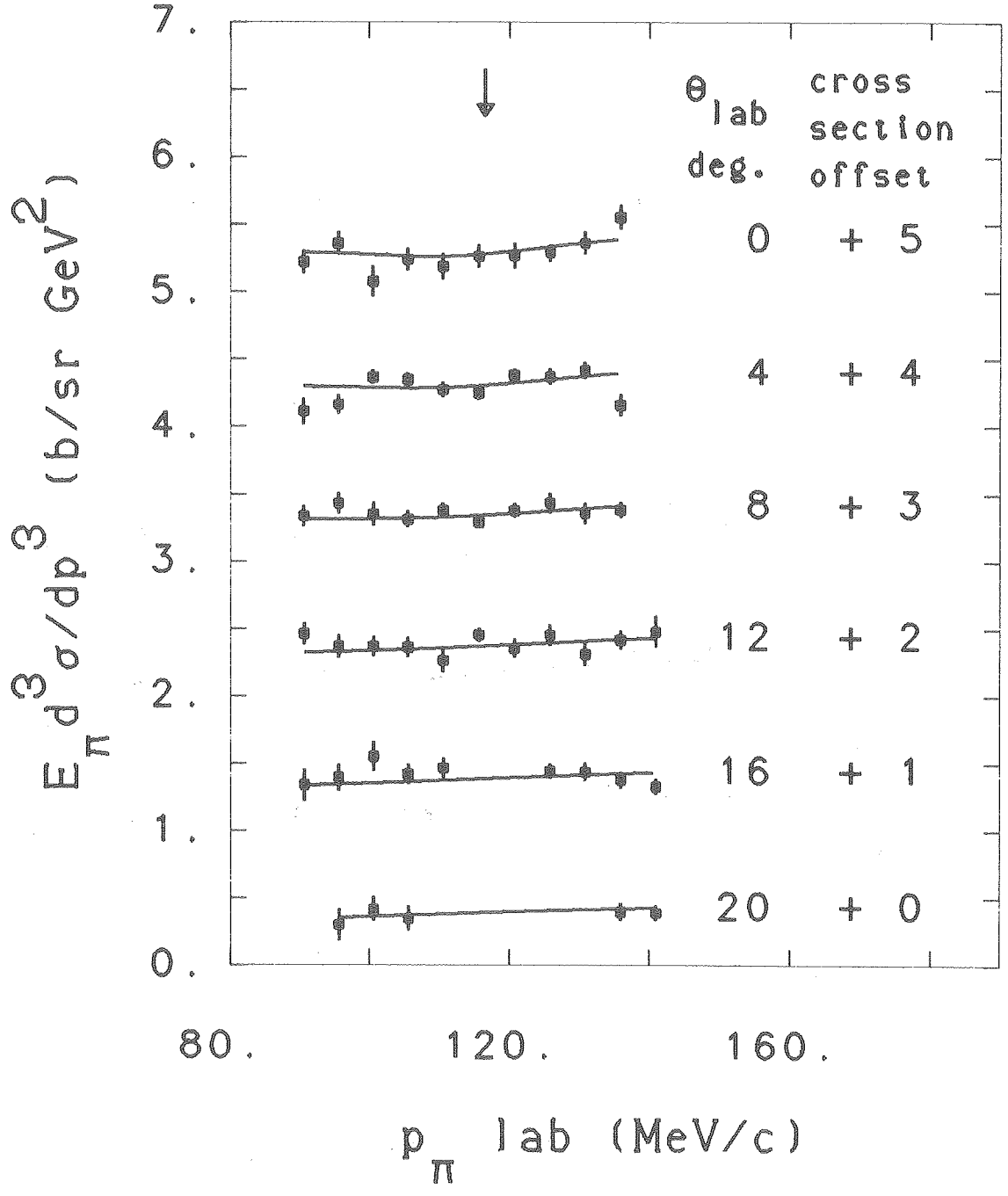
7.
6.
5.
4.
3.
2.
1.
0.
$E_\pi \frac{d^3\sigma}{dp^3}$ (b/sr GeV$^2$)
$\theta_{lab}$ deg.
cross section offset
0 + 5
4 + 4
8 + 3
12 + 2
16 + 1
20 + 0
80.
120.
160.
$p_\pi$ lab (MeV/c)
XBL 815-9943

Fig. 8B

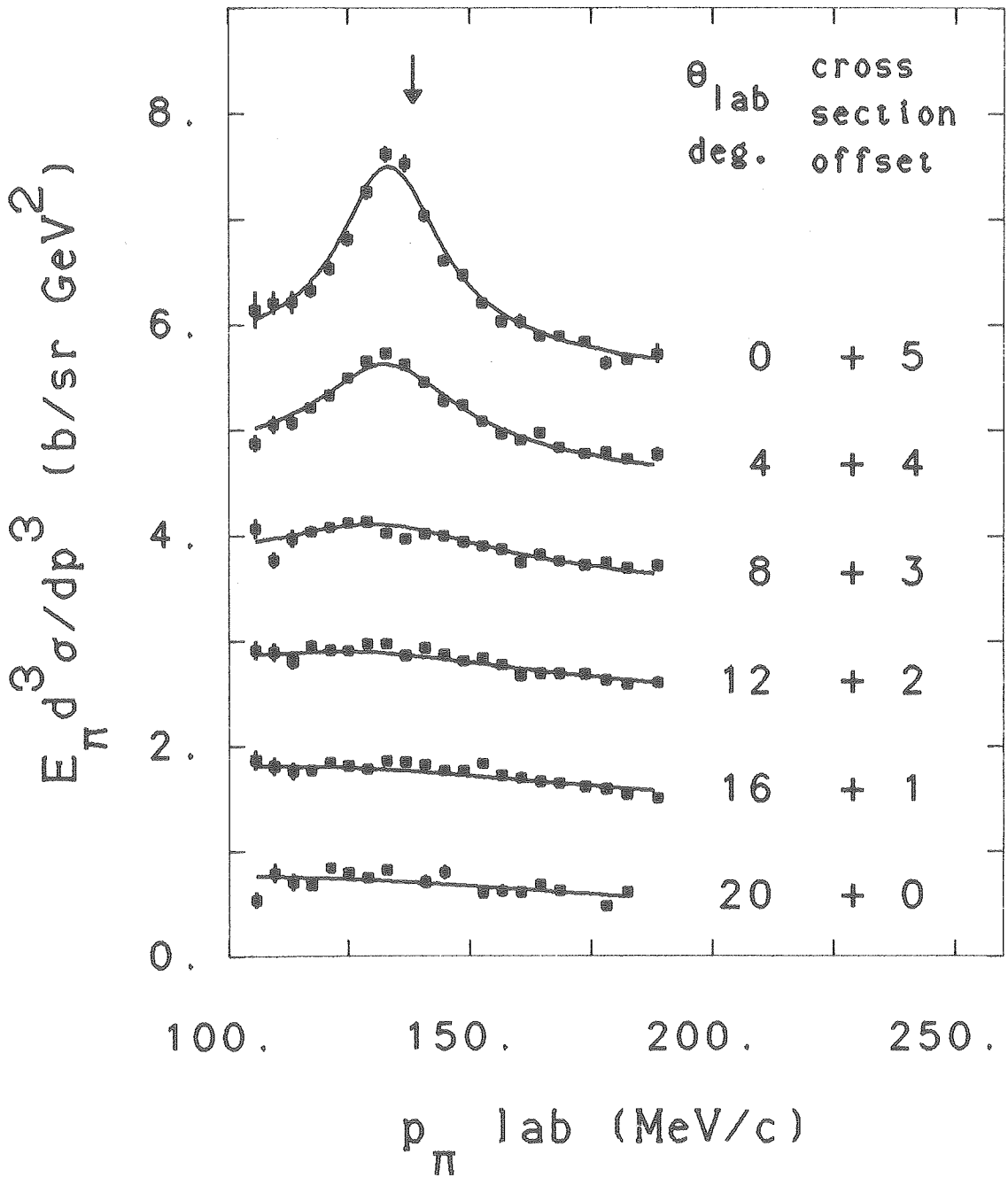


XBL 815-9944

Fig. 9A

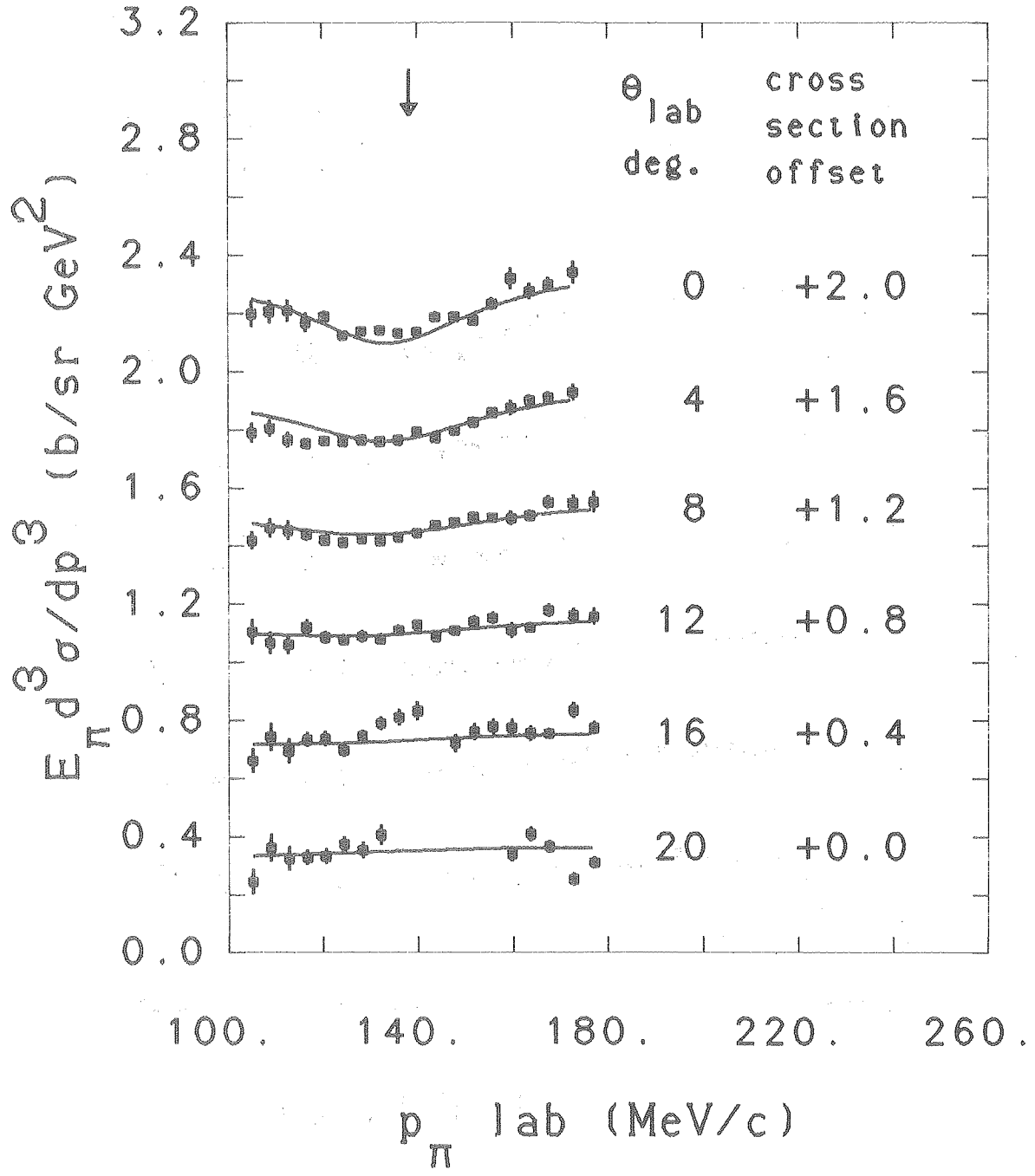


XBL 815-9947

Fig. 9B

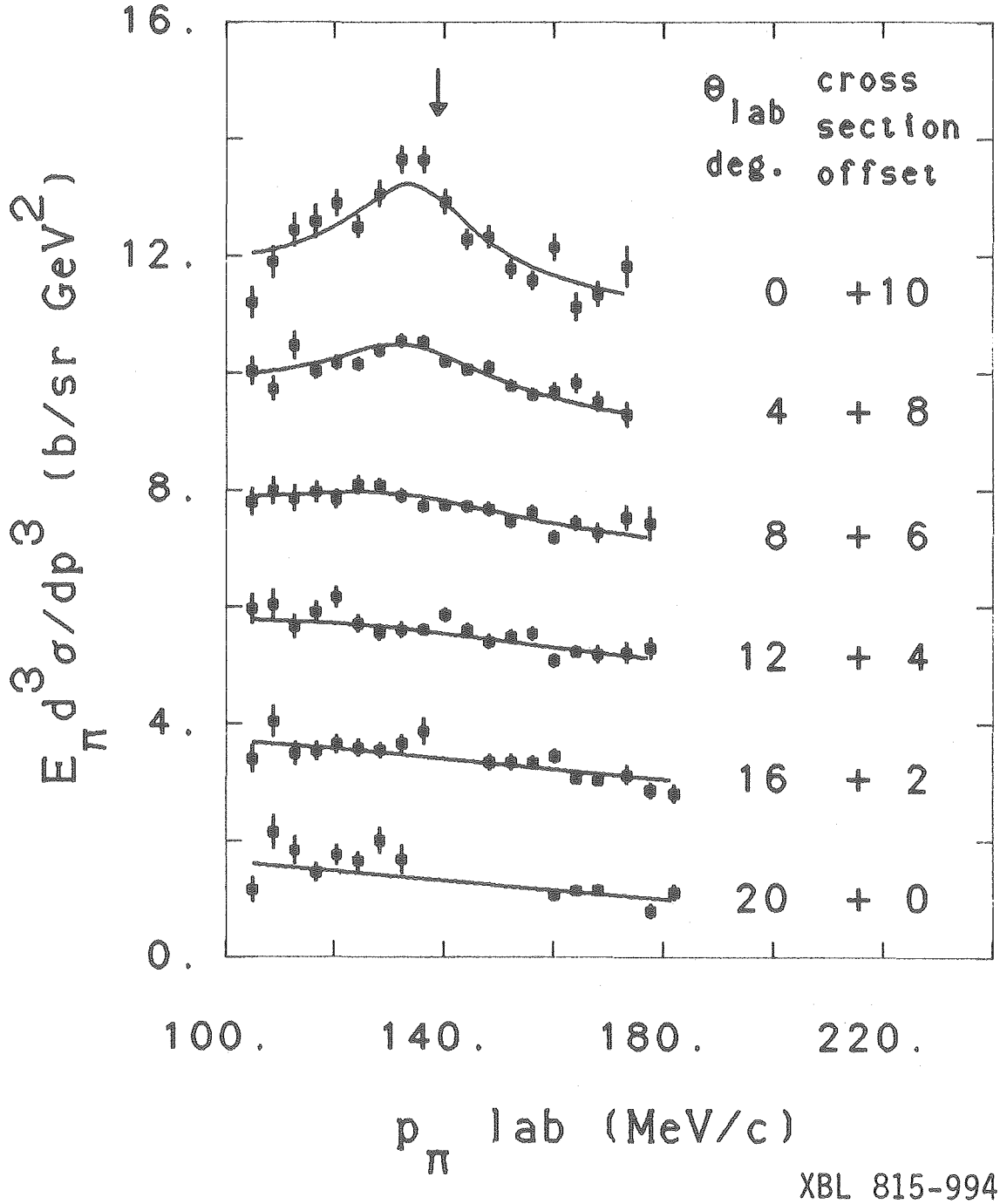
16.
12.
8.
4.
0.
$E_\pi \frac{d^3\sigma}{dp^3}$ (b/sr GeV$^2$)
$\theta_{lab}$ deg.
cross section offset
0 +10
4 + 8
8 + 6
12 + 4
16 + 2
20 + 0
100.
140.
180.
220.
$p_\pi$ lab (MeV/c)
XBL 815-9945

Fig. 10A

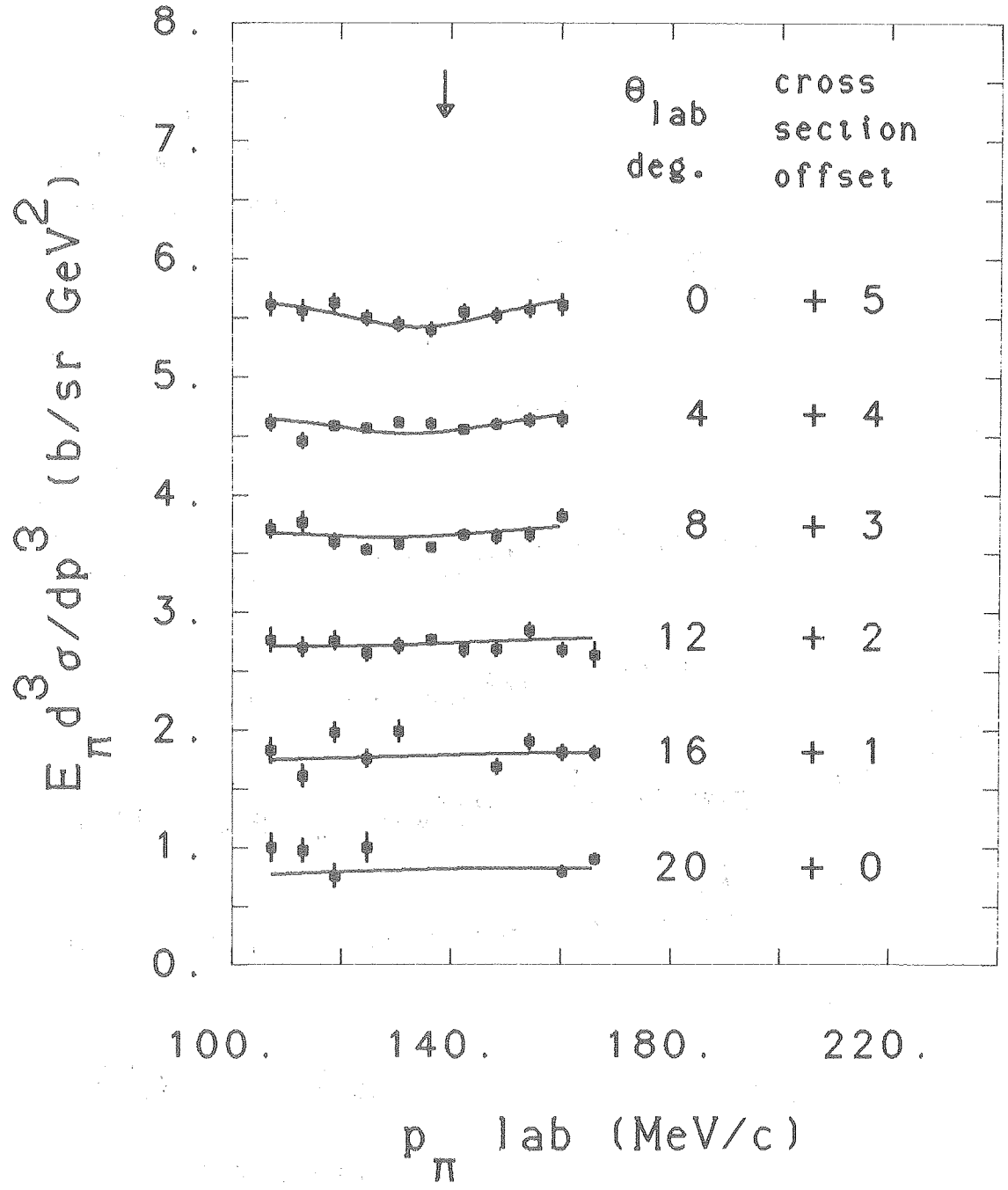
8.
7.
6.
5.
4.
3.
2.
1.
0.
$E_\pi \frac{d^3\sigma}{dp^3}$ (b/sr GeV$^2$)
$\theta_{lab}$ deg.
cross section offset
0 + 5
4 + 4
8 + 3
12 + 2
16 + 1
20 + 0
100.
140.
180.
220.
$p_\pi$ lab (MeV/c)
XBL 815-9948

Fig. 10B

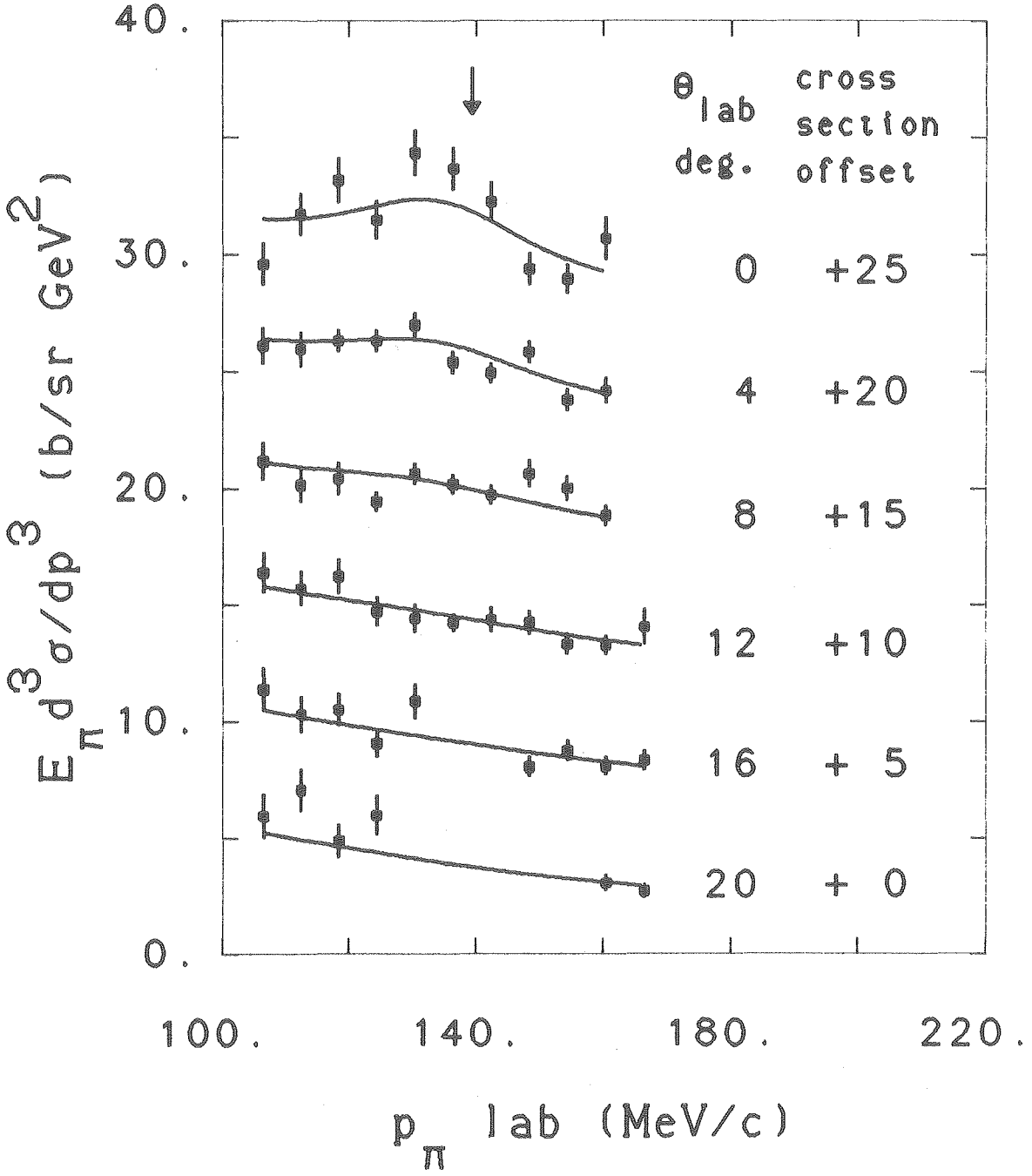
40.
30.
20.
10.
0.
$E_\pi d^3\sigma/dp^3$ (b/sr GeV$^2$)
$\theta_{lab}$ deg.
cross section offset
0 +25
4 +20
8 +15
12 +10
16 + 5
20 + 0
100.
140.
180.
220.
$p_\pi$ lab (MeV/c)
XBL 815-9946

Fig. 11A

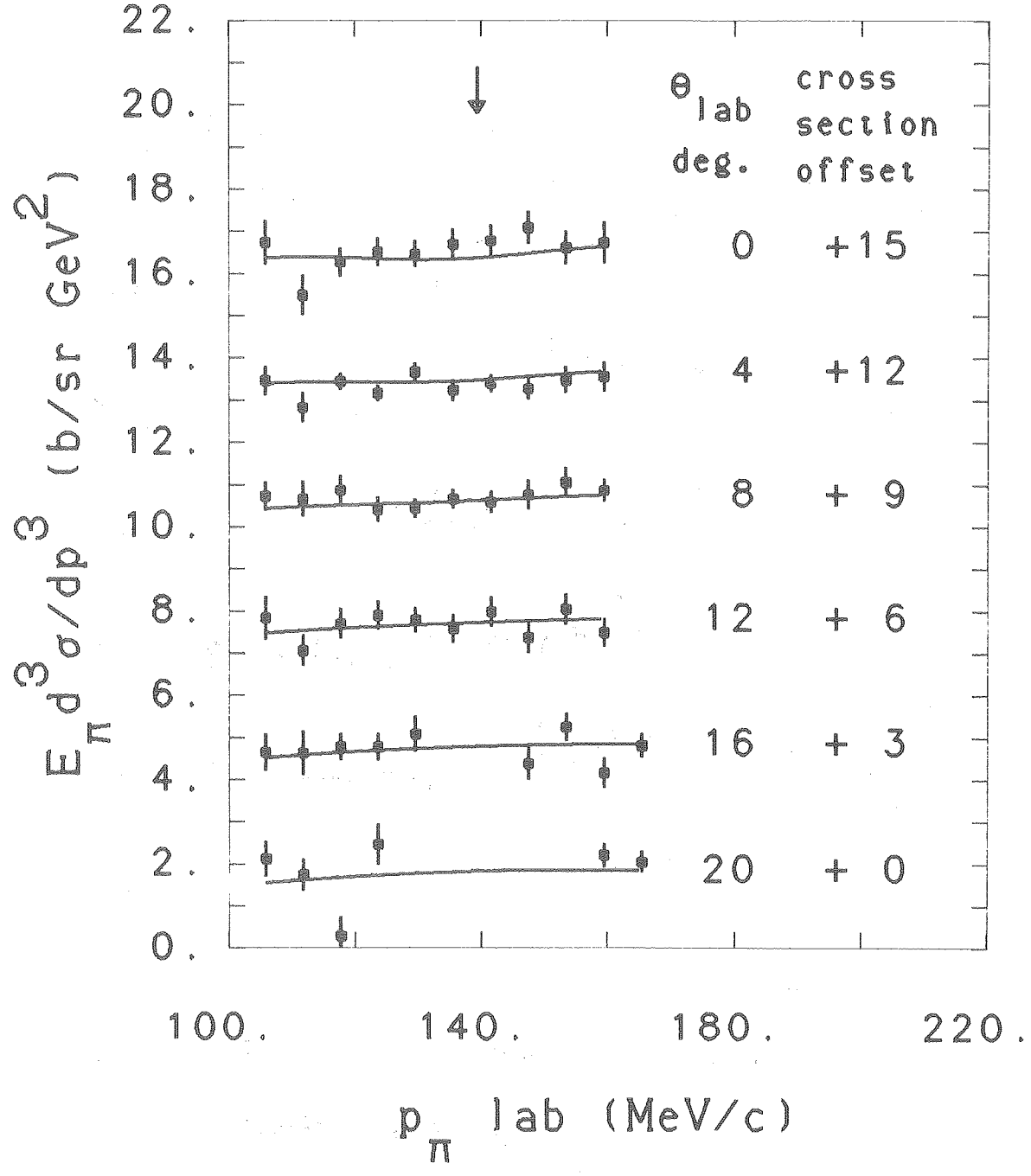


XBL 815-9949

Fig. 11B

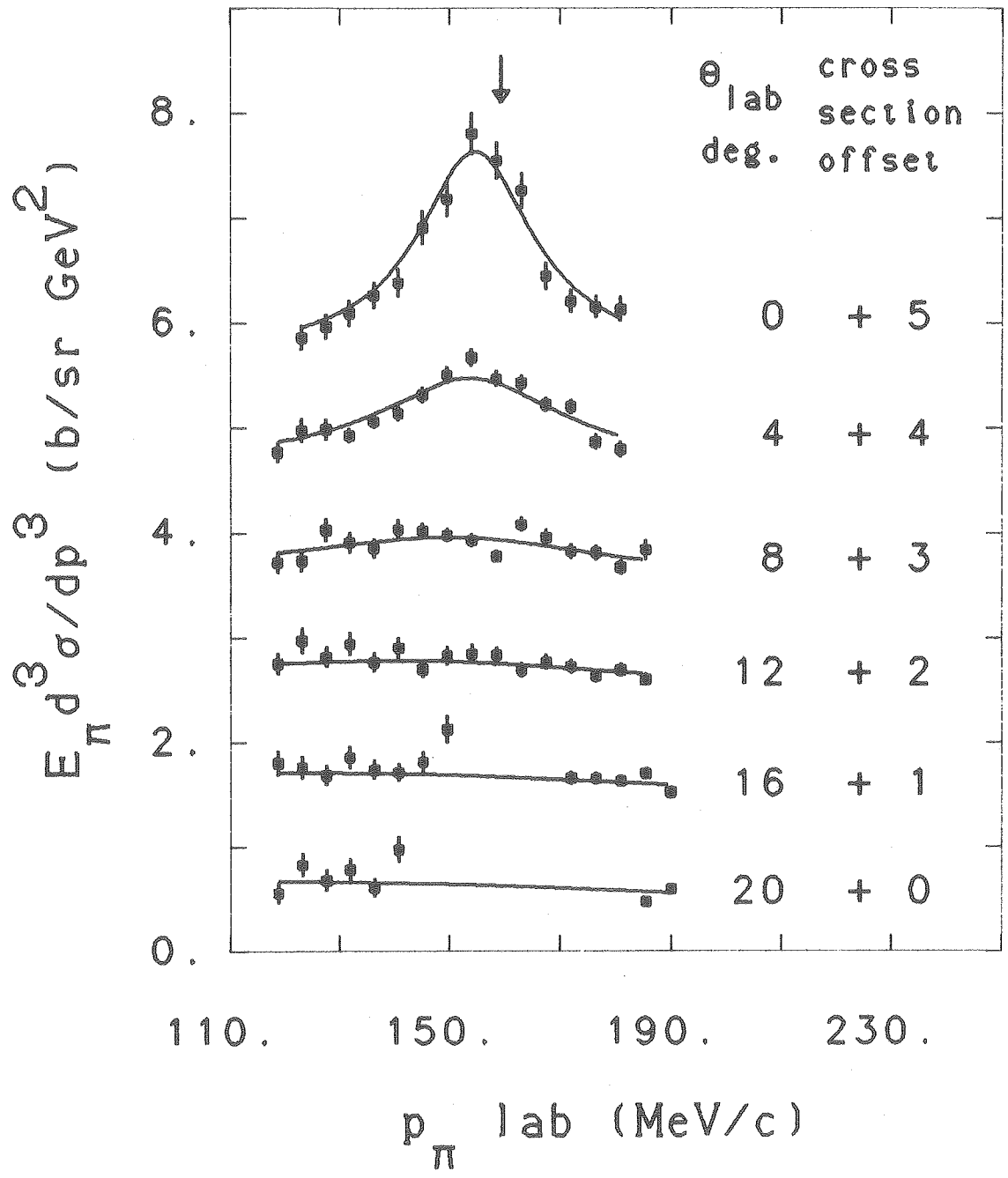
$E_\pi d^3\sigma/dp^3$ (b/sr GeV$^2$)
8.
6.
4.
2.
0.
$\theta_{lab}$ deg.
cross section offset
0 + 5
4 + 4
8 + 3
12 + 2
16 + 1
20 + 0
110.
150.
190.
230.
$p_\pi$ lab (MeV/c)
XBL 815-9950

Fig. 12A

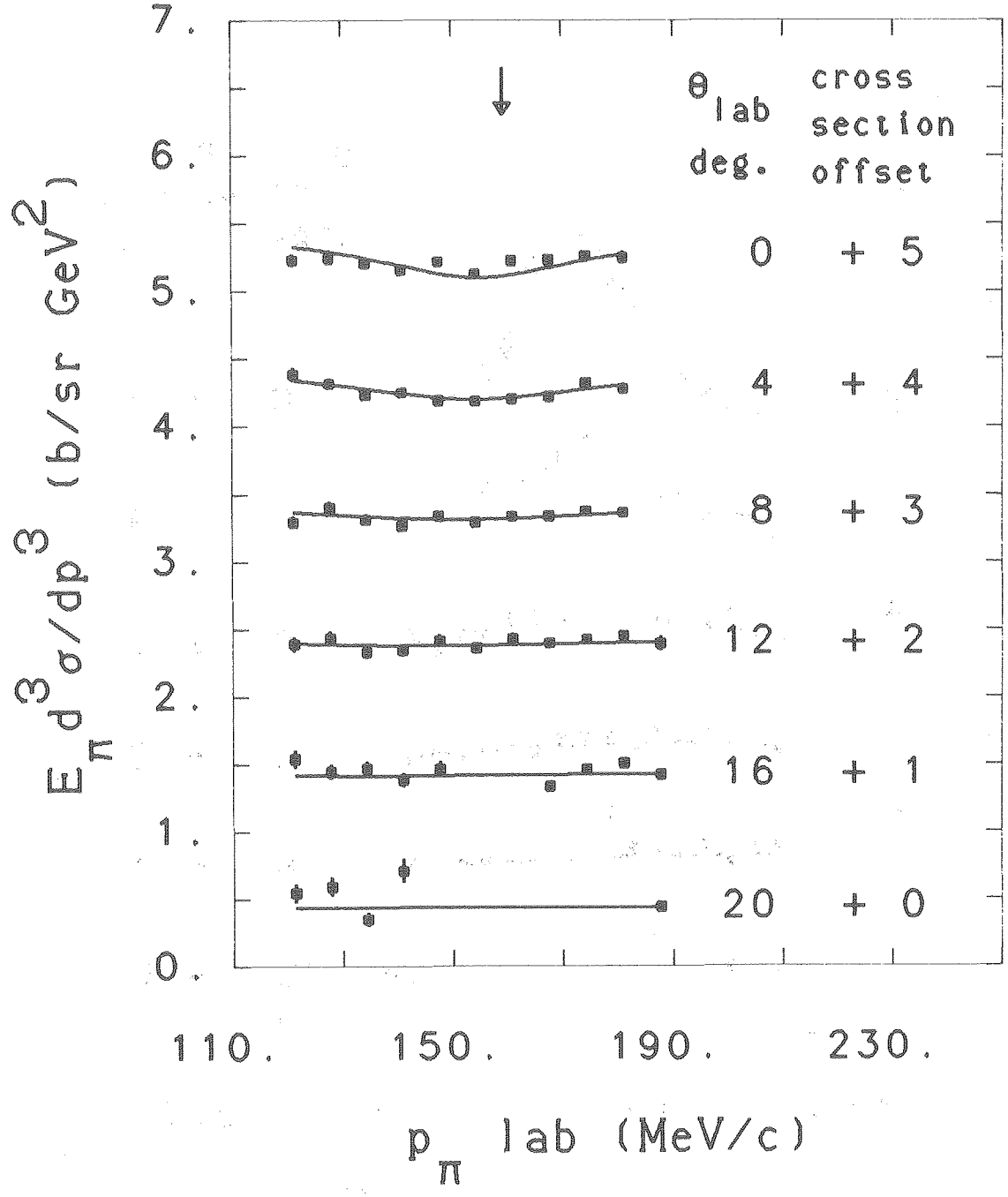
7.
6.
5.
4.
3.
2.
1.
0.
$E_\pi d^3\sigma/dp^3$ (b/sr GeV$^2$)
$\theta_{lab}$ deg.
cross section offset
0 + 5
4 + 4
8 + 3
12 + 2
16 + 1
20 + 0
110.
150.
190.
230.
$p_\pi$ lab (MeV/c)
XBL 815-9954

Fig. 12B

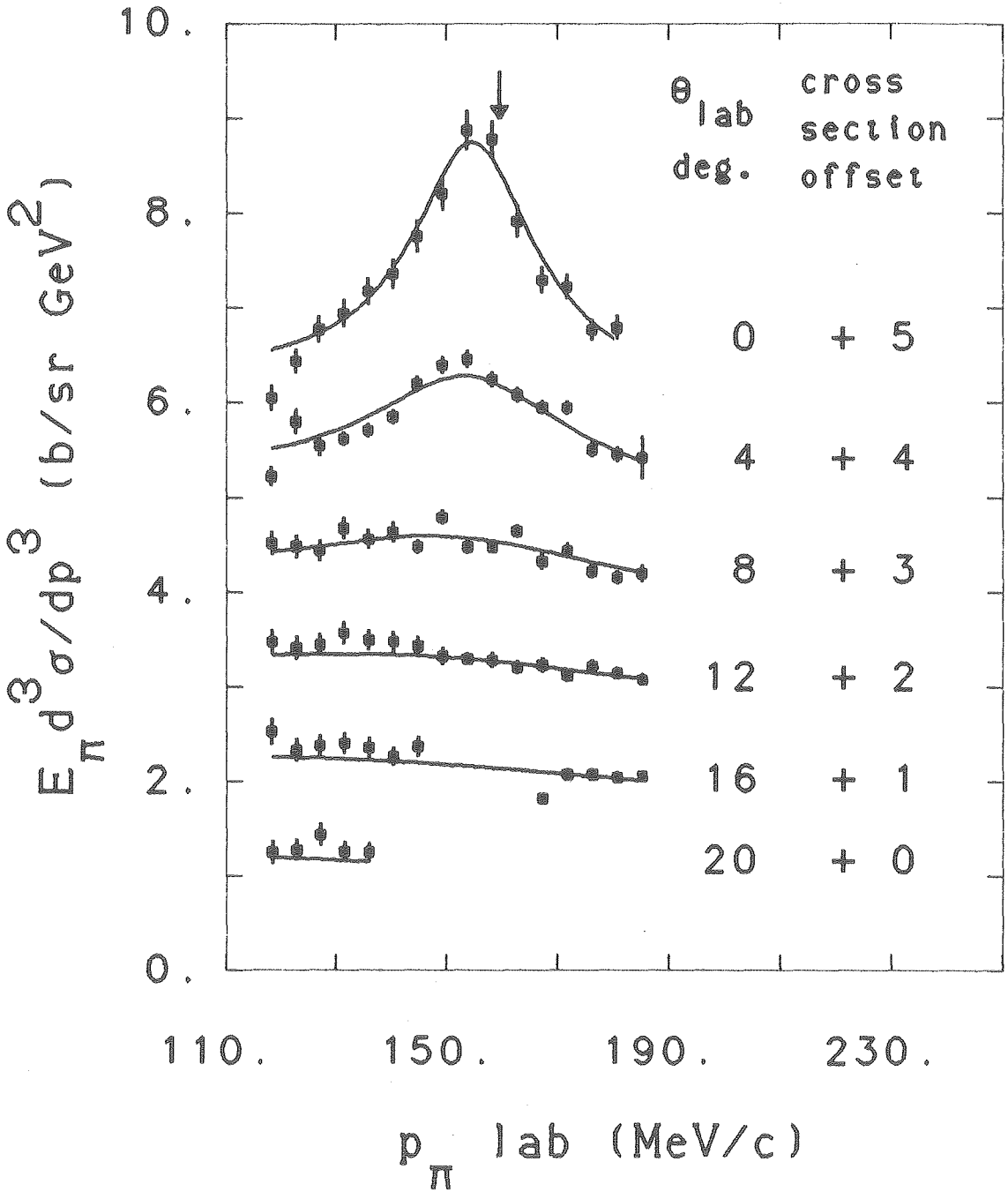


XBL 815-9951

Fig. 13A

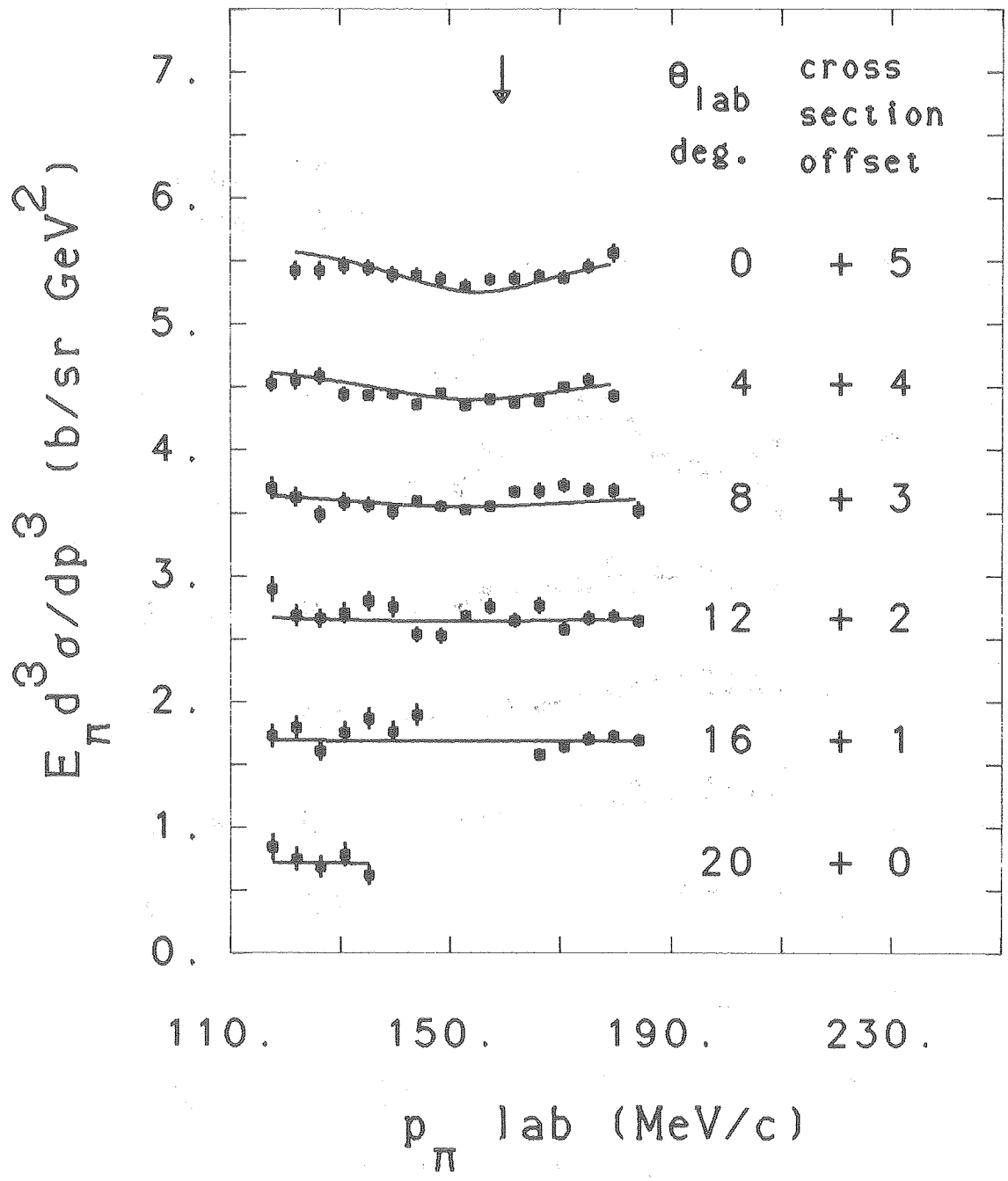
$E_\pi d^3\sigma/dp^3$ (b/sr GeV$^2$)
7.
6.
5.
4.
3.
2.
1.
0.
$\theta_{lab}$ deg.
cross section offset
0 + 5
4 + 4
8 + 3
12 + 2
16 + 1
20 + 0
110.
150.
190.
230.
$p_\pi$ lab (MeV/c)
XBL 815-9956

Fig. 13B

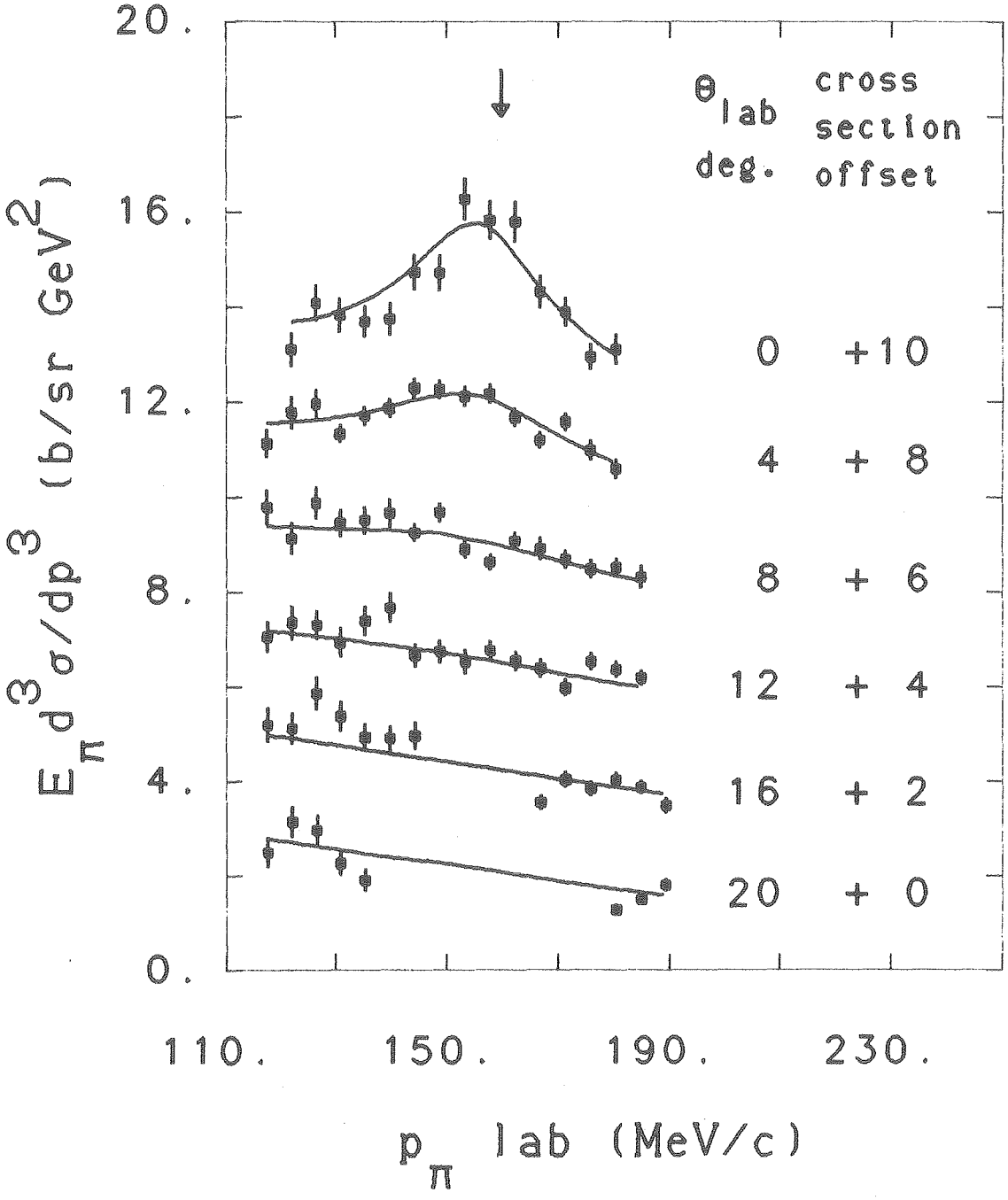


XBL 815-9952

Fig. 14A

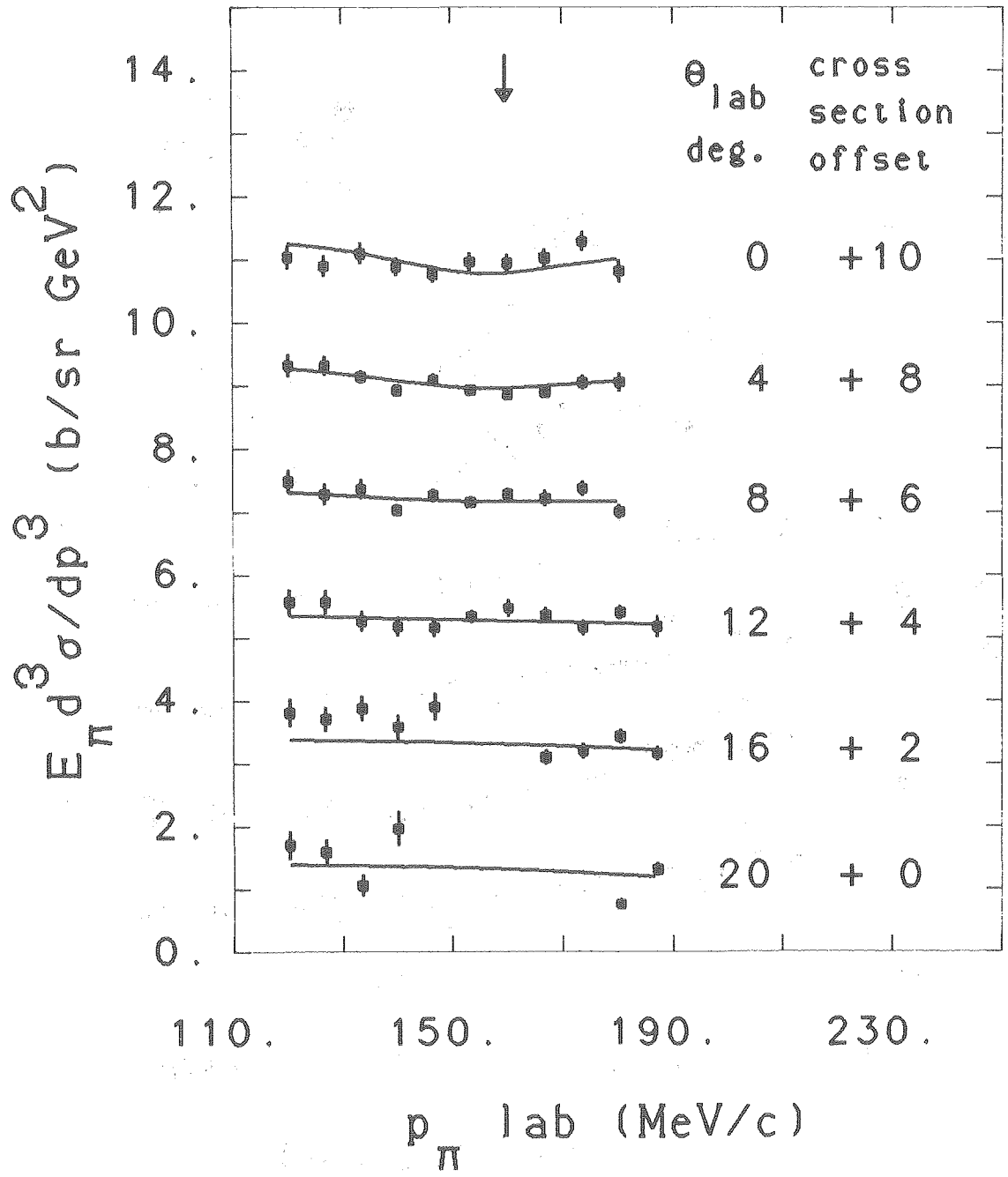
14.
12.
10.
8.
6.
4.
2.
0.
$E_\pi d^3\sigma/dp^3$ (b/sr GeV$^2$)
$\theta_{lab}$ deg.
cross section offset
0 +10
4 + 8
8 + 6
12 + 4
16 + 2
20 + 0
110.
150.
190.
230.
$p_\pi$ lab (MeV/c)
XBL 815-9957

Fig. 14B

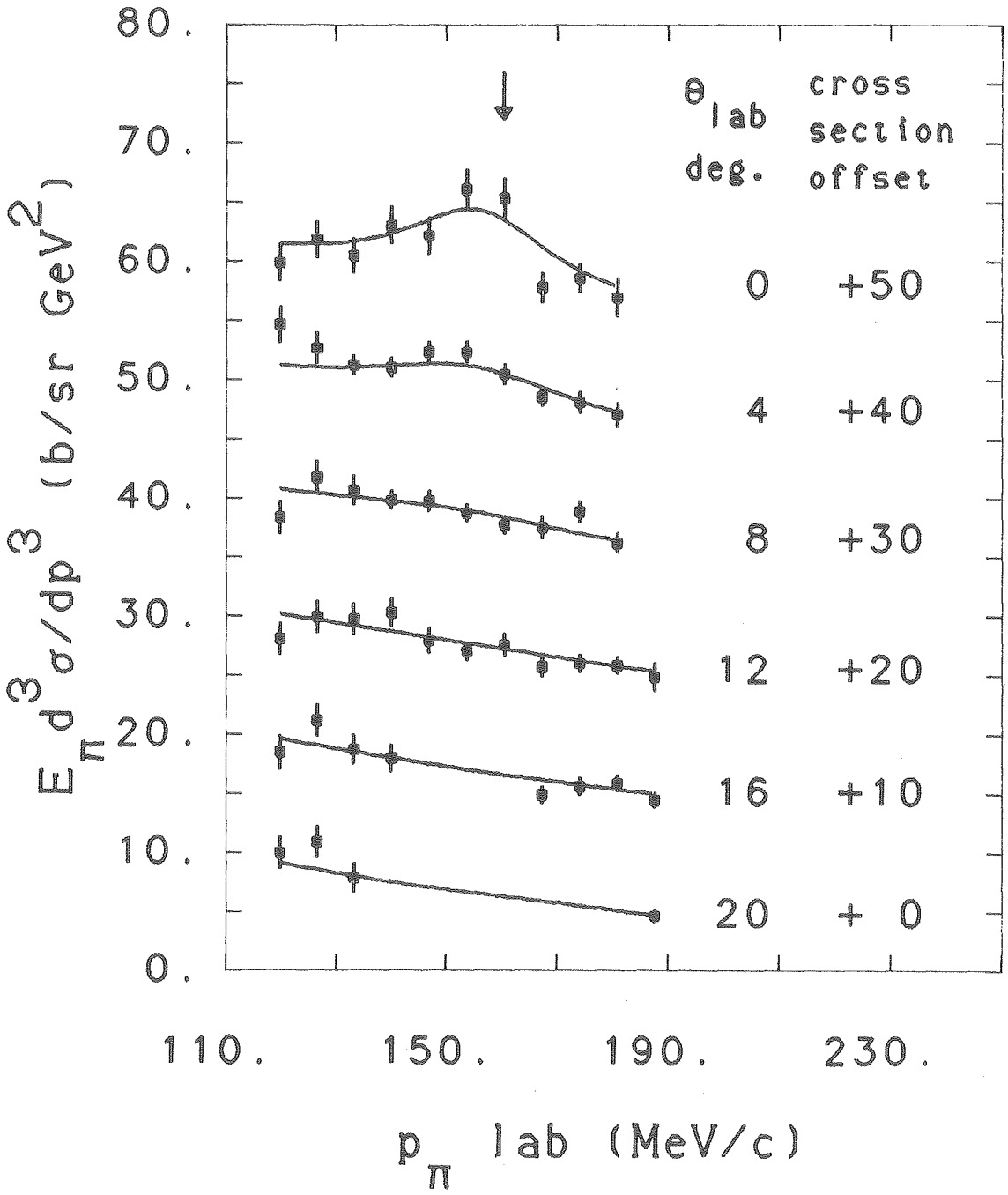
80.
70.
60.
50.
40.
30.
20.
10.
0.
$E_\pi \frac{d^3\sigma}{dp^3}$ (b/sr GeV$^2$)
$\theta_{lab}$ deg.
cross section offset
0 +50
4 +40
8 +30
12 +20
16 +10
20 + 0
110.
150.
190.
230.
$p_\pi$ lab (MeV/c)
XBL 815-9953

Fig. 15A

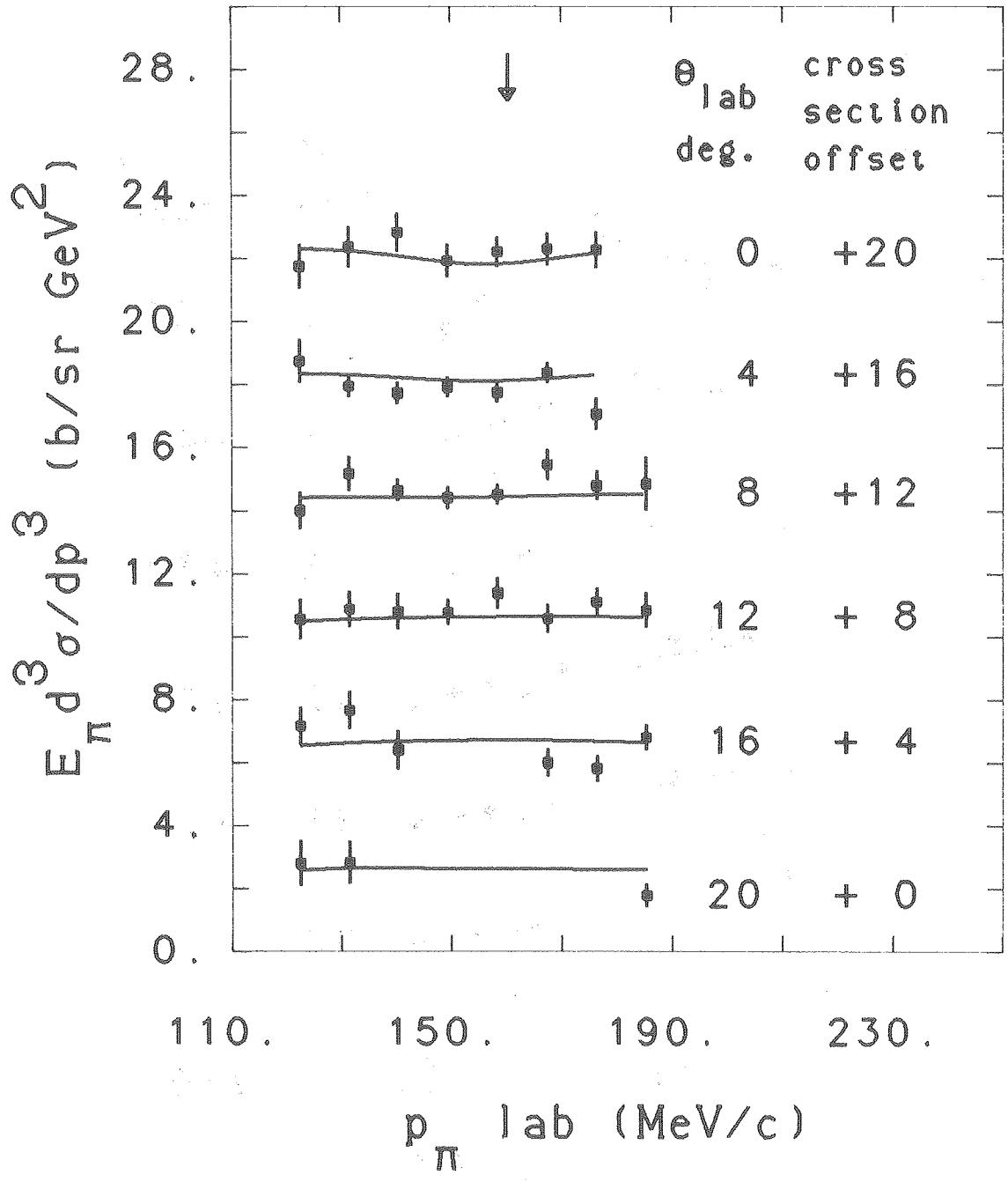
28.
24.
20.
16.
12.
8.
4.
0.
$E_\pi \frac{d^3\sigma}{dp^3}$ (b/sr GeV$^2$)
$\theta_{lab}$ deg.
cross section offset
0 +20
4 +16
8 +12
12 + 8
16 + 4
20 + 0
110.
150.
190.
230.
$p_\pi$ lab (MeV/c)
XBL 815-9955

Fig. 15B

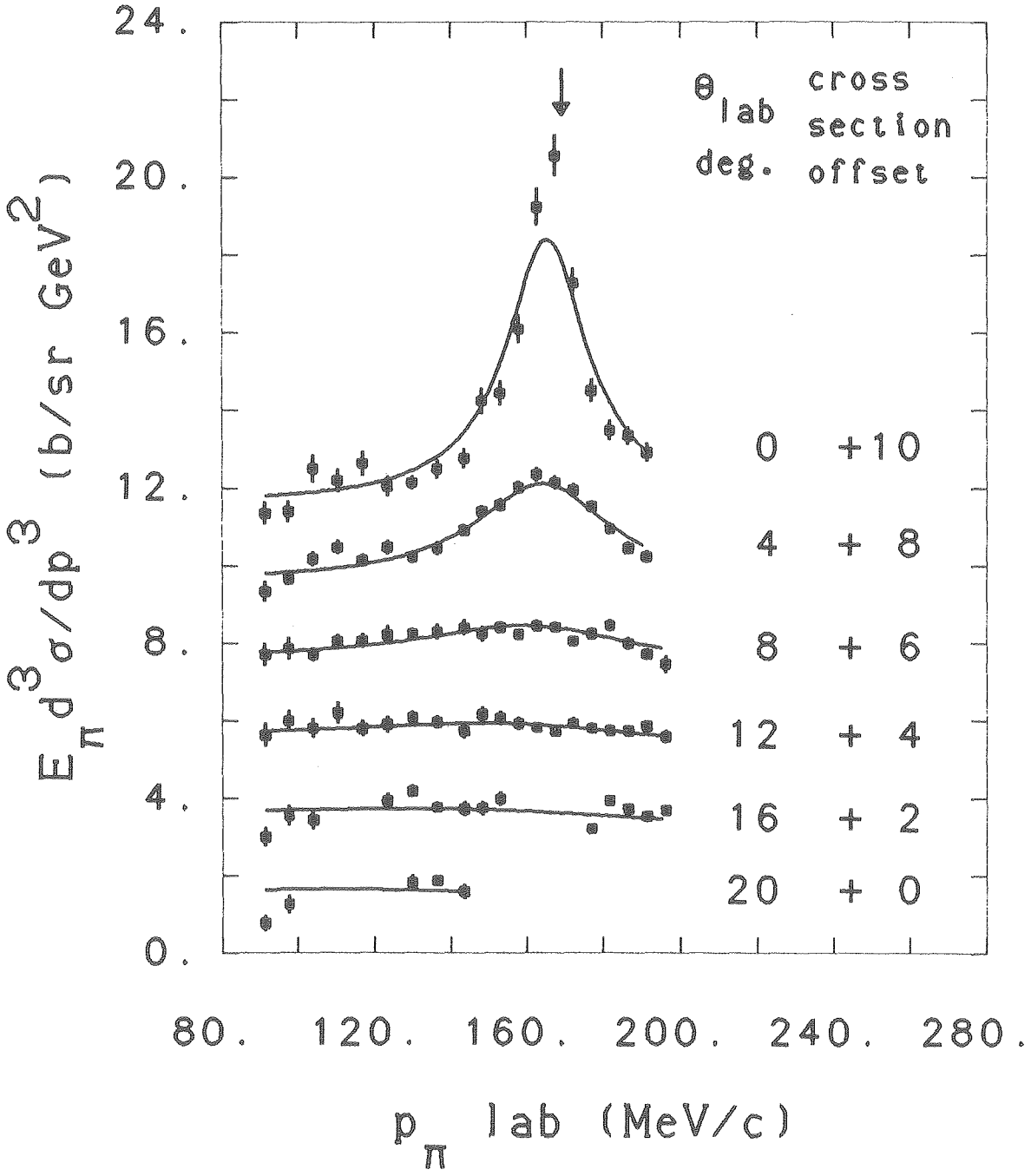
24.
20.
16.
12.
8.
4.
0.
$E_\pi \frac{d^3\sigma}{dp^3}$ (b/sr GeV$^2$)
$\theta_{lab}$ deg.
cross section offset
0 +10
4 + 8
8 + 6
12 + 4
16 + 2
20 + 0
80. 120. 160. 200. 240. 280.
$p_\pi$ lab (MeV/c)
XBL 815-9958

Fig. 16A

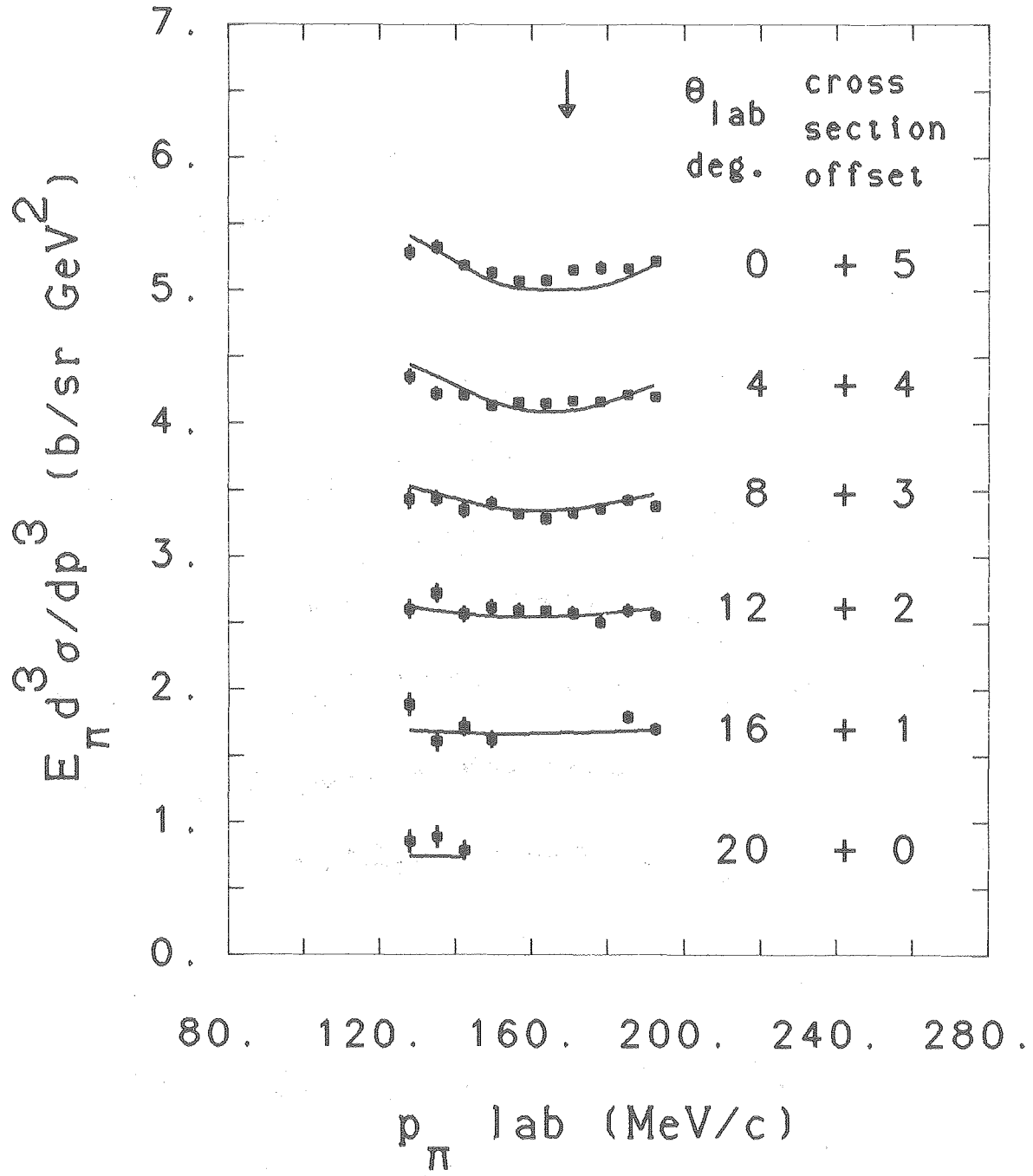
7.
6.
5.
4.
3.
2.
1.
0.
$E_\pi \frac{d^3\sigma}{dp^3}$ (b/sr GeV$^2$)
$\theta_{lab}$ deg.
cross section offset
0 + 5
4 + 4
8 + 3
12 + 2
16 + 1
20 + 0
80. 120. 160. 200. 240. 280.
$p_\pi$ lab (MeV/c)
XBL 815-9960

Fig. 16B

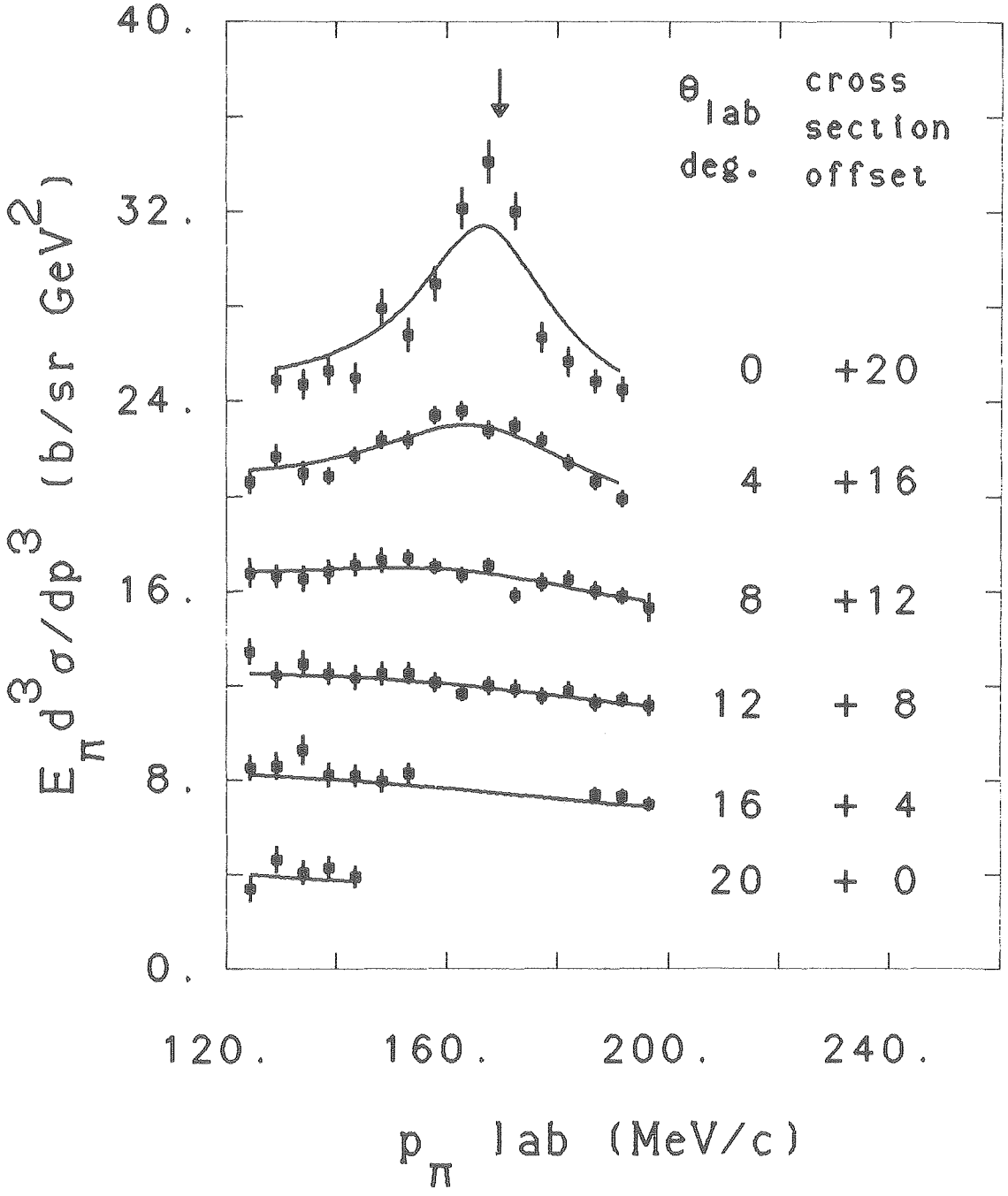


XBL 815-9959

Fig. 17A

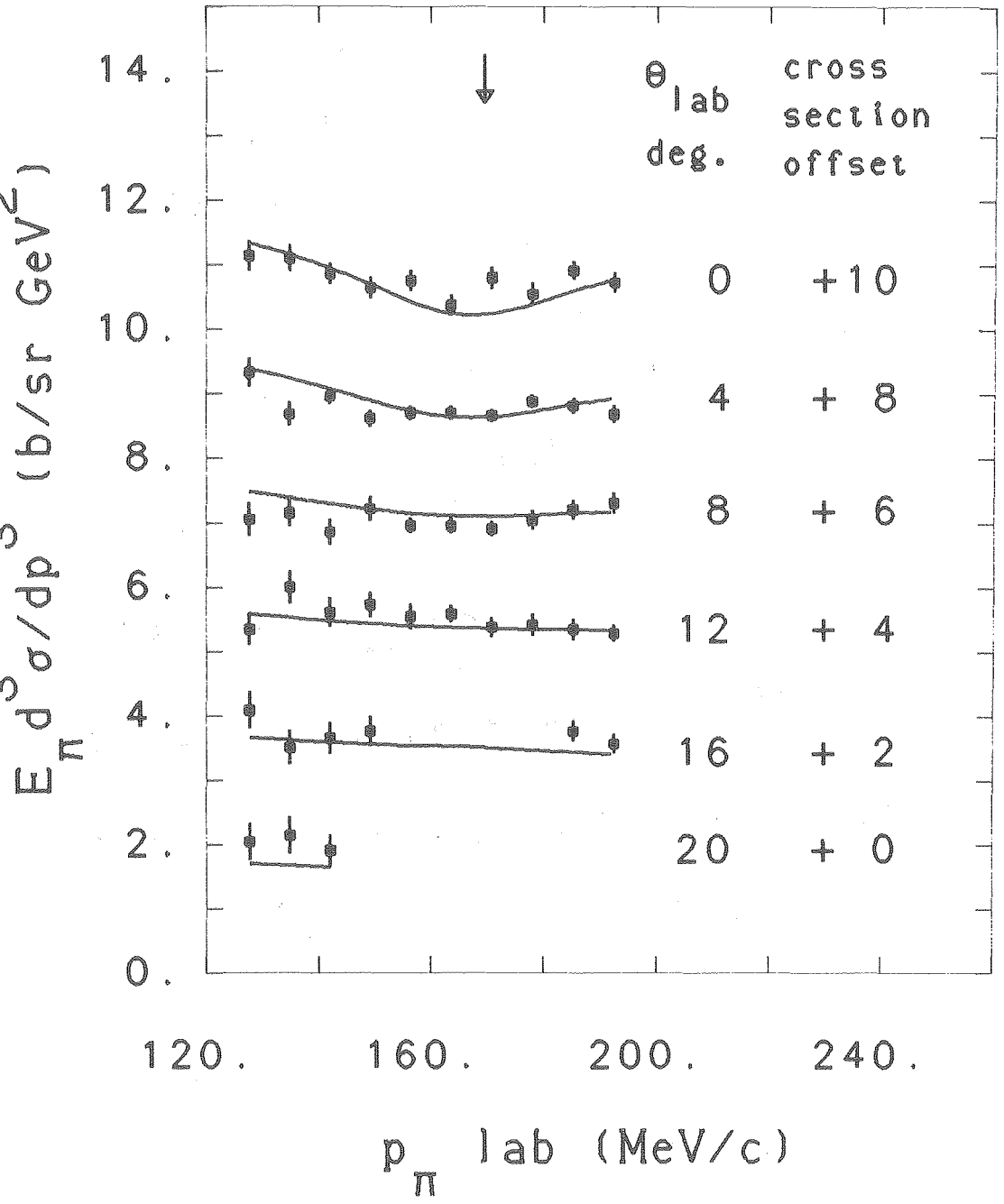
14.
12.
10.
8.
6.
4.
2.
0.
$E_\pi \frac{d^3\sigma}{dp^3}$ (b/sr GeV$^2$)
$\theta_{lab}$ deg.
cross section offset
0 +10
4 + 8
8 + 6
12 + 4
16 + 2
20 + 0
120.
160.
200.
240.
$p_\pi$ lab (MeV/c)
XBL 815-9961

Fig. 17B

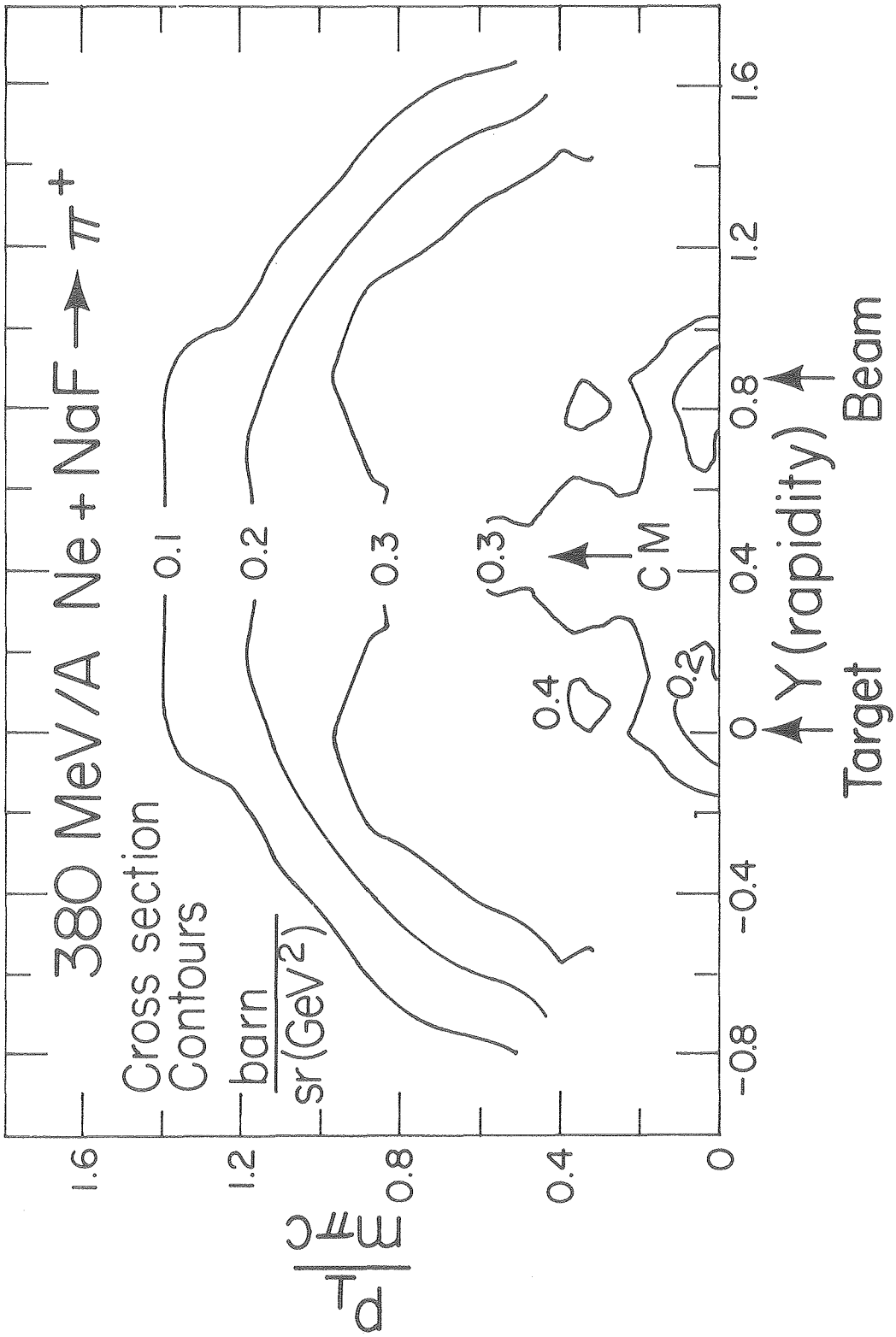


XBL815-2270

Fig. 18

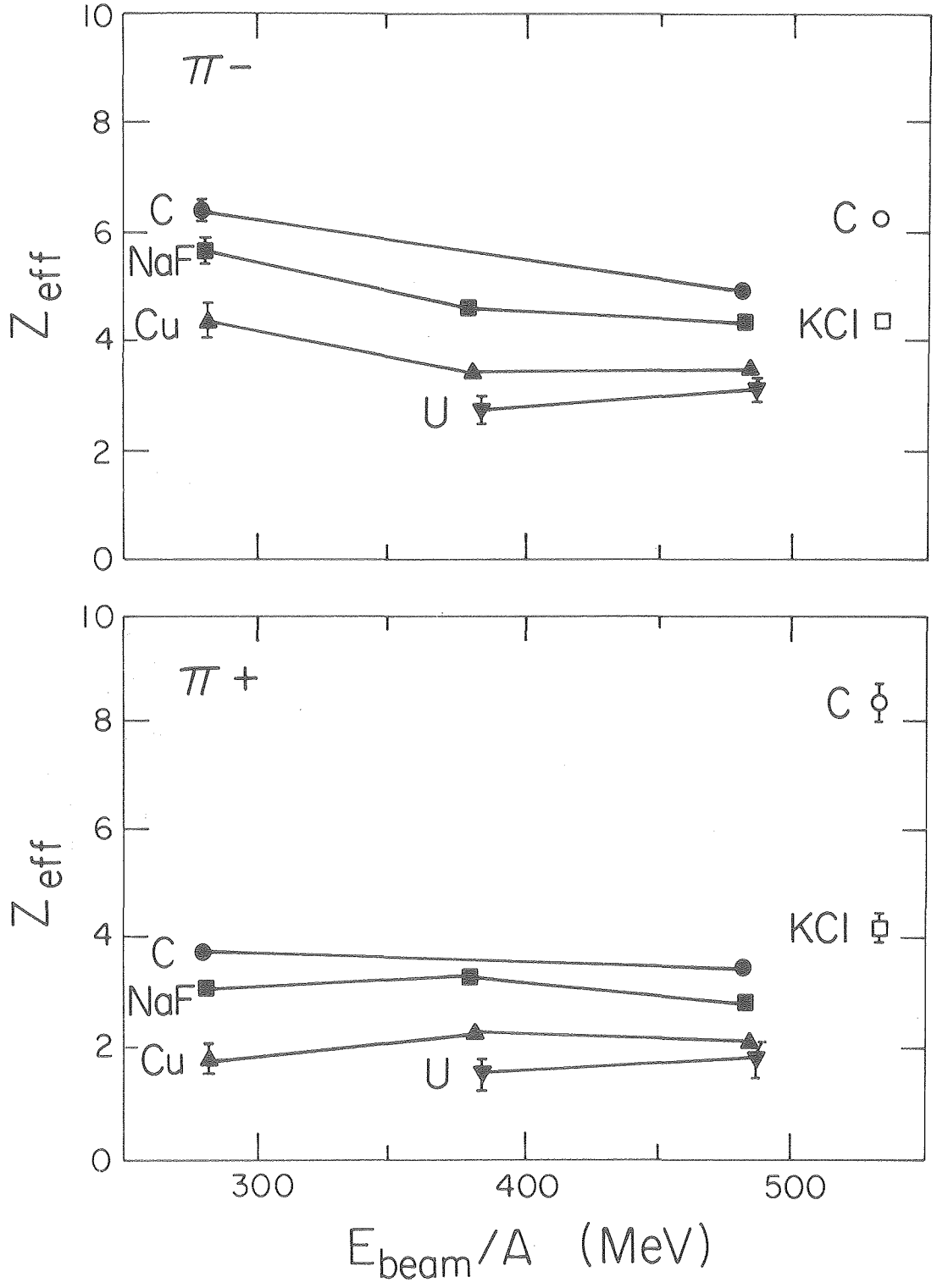


XBL 816-2335

Fig. 19

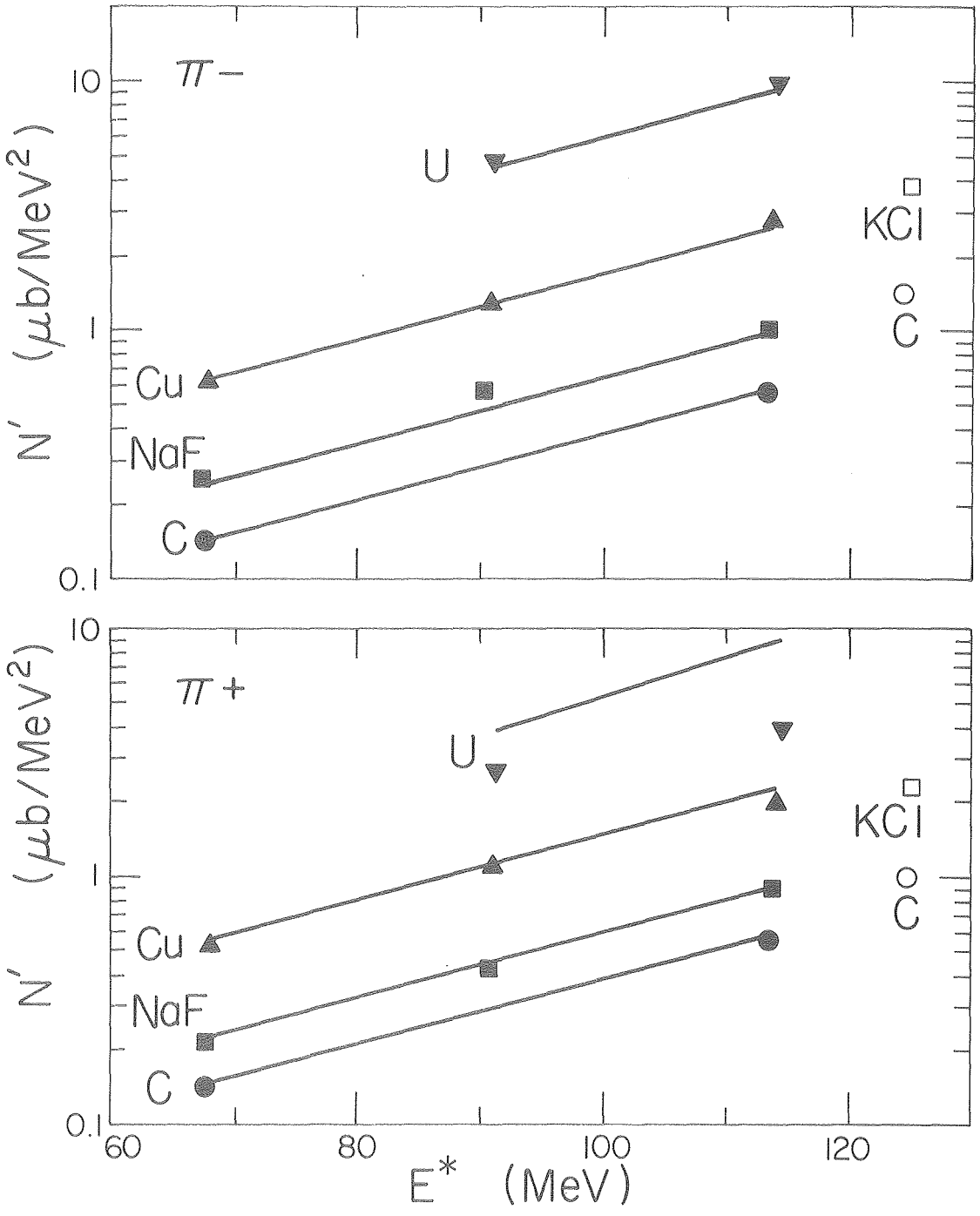


XBL 816-2336

Fig. 20